Inorganic Chemistry

Article

pubs.acs.org/IC

Semiconducting Tin and Lead Iodide Perovskites with Organic Cations: Phase Transitions, High Mobilities, and Near-Infrared Photoluminescent Properties

Constantinos C. Stoumpos, Christos D. Malliakas, and Mercouri G. Kanatzidis*

Department of Chemistry, Northwestern University, Evanston, Illinois 60208, United States

Supporting Information

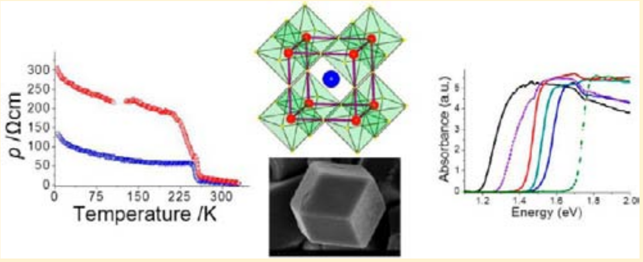

ABSTRACT: A broad organic−inorganic series of hybrid metal iodide perovskites with the general formulation AMI_3, where A is the methylammonium ($CH_3NH_3^+$) or formamidinium ($HC(NH_2)_2^+$) cation and M is Sn (**1** and **2**) or Pb (**3** and **4**) are reported. The compounds have been prepared through a variety of synthetic approaches, and the nature of the resulting materials is discussed in terms of their thermal stability and optical and electronic properties. We find that the chemical and physical properties of these materials strongly depend on the preparation method. Single crystal X-ray diffraction analysis of **1**−**4** classifies the compounds in the perovskite structural family. Structural phase transitions were observed and investigated by temperature-dependent single crystal X-ray diffraction in the 100−400 K range. The charge transport properties of the materials are discussed in conjunction with diffuse reflectance studies in the mid-IR region that display characteristic absorption features. Temperature-dependent studies show a strong dependence of the resistivity as a function of the crystal structure. Optical absorption measurements indicate that **1**−**4** behave as direct-gap semiconductors with energy band gaps distributed in the range of 1.25−1.75 eV. The compounds exhibit an intense near-IR photoluminescence (PL) emission in the 700−1000 nm range (1.1−1.7 eV) at room temperature. We show that solid solutions between the Sn and Pb compounds are readily accessible throughout the composition range. The optical properties such as energy band gap, emission intensity, and wavelength can be readily controlled as we show for the isostructural series of solid solutions $CH_3NH_3Sn_{1-x}Pb_xI_3$ (**5**). The charge transport type in these materials was characterized by Seebeck coefficient and Hall-effect measurements. The compounds behave as *p*- or *n*-type semiconductors depending on the preparation method. The samples with the lowest carrier concentration are prepared from solution and are *n*-type; *p*-type samples can be obtained through solid state reactions exposed in air in a controllable manner. In the case of Sn compounds, there is a facile tendency toward oxidation which causes the materials to be doped with Sn^{4+} and thus behave as *p*-type semiconductors displaying metal-like conductivity. The compounds appear to possess very high estimated electron and hole mobilities that exceed 2000 $cm^2/(V\ s)$ and 300 $cm^2/(V\ s)$, respectively, as shown in the case of $CH_3NH_3SnI_3$ (**1**). We also compare the properties of the title hybrid materials with those of the "all-inorganic" $CsSnI_3$ and $CsPbI_3$ prepared using identical synthetic methods.

INTRODUCTION

Main group metal halometallates in general and iodometallates in particular, represent a large class of semiconducting materials which display intriguing optical and electronic properties. Of special interest are the group 14 iodometalates, since they can adopt perovskitic structures that are amenable to compositional variation.[1] When the A-site in the perovskite formula, AMI_3, is occupied by a small monovalent cation, such as Rb, Cs, methylammonium, or formanidinium, a three-dimensional (3D) framework is obtained.[2] If a larger cation is used instead two-dimensional (2D) layered,[3] or one-dimensional (1D) chain[4] materials are obtained with formulas AMI_3, A_2MI_4, and A_3MI_5 which still retain their perovskite (or corner sharing) connectivity. 0D A_2SnI_6 and A_4PbI_6 perovskites have also been obtained.[5] The stoichiometry of the final material and the metal-iodide linkages are extremely sensitive to the nature of the cation with both size and functionality playing a crucial role.[6] The connectivity of the MI_6 octahedra is also affected varying from corner-sharing to edge-sharing to face-sharing.[6] The structural diversity of these compounds has been reviewed.[7] Among these there are some remarkable series of materials with the general formulas $(RNH_3)_2(CH_3NH_3)_{n-1}Sn_nI_{3n+1}$,[8] (with n = 1−5) and $IC(NH_2)_2(CH_3NH_3)_mSn_mI_{3m+2}$ (with m = 2−4),[9] which was reported to display a stepwise increase in conductivity with increasing n or m, reaching its maximum value for the pure $CH_3NH_3SnI_3$ perovskite. However, the isostructural compounds of lead, $(RNH_3)_2(CH_3NH_3)_{n-1}Pb_nI_{3n+1}$,[10] show a much different behavior, displaying a very strong exciton-binding in the excited state. The energy bandgap of these semiconductors can be easily tuned across a wide range of

Received: May 15, 2013
Published: July 8, 2013

dx.doi.org/10.1021/ic401215x | *Inorg. Chem.* 2013, 52, 9019−9038

energies by modifying either the dimensionality of the inorganic framework or the functionality of the organic cation (or both), and this is responsible for their unique properties. Photoconductivity,[2b] ionic conductivity,[11] electrical conductivity,[8,9,12] photo-[3c] and electroluminescence,[13] exciton formation,[10,14] and phase transitions[2] are but a few properties giving rise to applications ranging from thin film transistors (TFTs)[3e] to solar energy conversion.[15] Moreover, the nonperovskite structures also can exhibit interesting phenomena such ferroelectricity[6i,16] and nonlinear optical properties.[6d] Solution processability of such materials is another key property which makes them very attractive for device applications such as all-solid state dye-sensitized solar cells.[15c,17]

Our interest in these materials arose from the observation that $CsSnI_3$,[18] in its perovskite modification,[2g] displays intense room temperature photoluminescence (PL) in the near-infrared spectral region when excited with a 532 nm (Nd:YAG, frequency doubled) laser beam.[19] In addition, the success of the $CsSnI_3$ in enabling the efficient all solid state dye-sensitized solar cell motivated us to study the broader family of these perovskites as they too are expected to perform similarly. We have been studying the parent compound $CsSnI_3$[12,15] while simultaneously working on hybrid perovskite analogues which we describe here. In this article we report the synthesis and a broad set of physical properties of $CH_3NH_3SnI_3$ (**1**),[2d,i,j,8] $HC(NH_2)_2SnI_3$ (**2**),[9b] $CH_3NH_3PbI_3$ (**3**),[2e,3b,14,20] $HC(NH_2)_2PbI_3$ (**4**), and the solid solutions $CH_3NH_3Sn_{1-x}Pb_xI_3$ (**5**) with $x = 0.25$ (**5a**), $x = 0.50$ (**5b**), and $x = 0.75$ (**5c**). Our studies focus on the structural, electrical, and optical properties of the materials and how they are affected by the inherent structural phase transitions and/or by the level of impurities. The latter vary based on synthetic route. For comparison purposes, we also prepared the cesium analogues $CsSnI_3$ (**6**),[2f,g] and $CsPbI_3$ (**7**)[2c,h] to pinpoint the differences and similarities with the related hybrid perovskites reported here. We show that the level of impurities is critical and determines the final physical/chemical properties of the materials. Precisely because of this tendency it is possible to tune/optimize the remarkable emission properties of the materials as we successfully show in the case of the solid solution **5**. The Sn analogues exhibit the very rare characteristic of being simultaneously good electrical conductors and intense room temperature photoluminescent materials at near-infrared wavelengths.

EXPERIMENTAL SECTION

Synthesis. Experimental details and synthetic procedures for the synthesis of **1**−**5** can be found in the Supporting Information.[21]

Optical Spectroscopy. Optical diffuse-reflectance measurements were performed at room temperature using a Shimadzu UV-3101 PC double-beam, double-monochromator spectrophotometer operating from 200 to 2500 nm. $BaSO_4$ was used as a nonabsorbing reflectance reference. The generated reflectance-versus-wavelength data were used to estimate the band gap of the material by converting reflectance to absorbance data according to the Kubelka−Munk equation: $\alpha/S = (1 - R)^2/2R$, where R is the reflectance and α and S are the absorption and scattering coefficients, respectively.[22]

PL Measurements. The samples were measured using an OmniPV Photoluminescence system, equipped with a DPSS frequency-doubling Nd:YAG laser (500 mW power output, class 4) emitting at 532 nm coupled with a bundle of 8 400 μm-core optical fibers as an excitation source. The emission was measured in the 200−1700 nm range with two StellarNet spectrometers, covering the 200−850 nm (CCD) and 900−1700 nm (InGaAs) areas, coupled with 400 μm-core optical fibers and integrated within the bundle (10 optical fibers total). The backscattered light is collected at ∼180° angle at 3 mm from the sample. For estimating the intensity of the signal and also to account for the excitation beam fluctuations, a disk of single-crystalline InP (930 nm emission peak) was measured before and after the sample measurements. The excitation time used was 100 ms, and the data were averaged for 5 independent scans. The data were analyzed using the SpectraWiz or the OmniPV_PL software.[23]

Vibrational Spectroscopy. Fourier-transformed infrared spectra (FT-IR) were recorded on a Nicolet 6700 IR spectrometer in the 400−4000 cm^{-1} spectral region using a diffuse-reflectance kit. The measurement is conducted under a constant flow of nitrogen. The spectrum is referenced toward a metal mirror used as the 100% reflectance standard.

Charge Transport Properties. *(a). Low Temperature Resistivity Measurements.* Four-probe low temperature measurements were performed on a Quantum Design PPMS device in 5−330 K temperature range using the four-probe technique on well-defined rhombic dodecahedral single-crystals grown from the solution method. Current was applied on a rhombic face of the crystal, and the voltage was measured on two of the apexes of the polyhedron (c-axis). The resistance was recorded as an average of both negative and positive current polarities.

(b). High Temperature Resistivity and Seebeck Coefficient and Hall-Effect Measurements. Four-probe room and high temperature measurements were performed in the 300−550 K range. Measurements were made for arbitrary current directions in the ab-plane using standard point contact geometry. A homemade resistivity apparatus equipped with a Keithley 2182A nanovoltometer, Keithley 617 electrometer, Keithley 6220 Precision direct current (DC) source, and a high temperature vacuum chamber controlled by a K-20 MMR system was used. Data acquisition was controlled by custom written software. This setup is referred to as “conventional” throught the text.

Seebeck measurements were performed in the 300−550 K temperature range on the same homemade apparatus using Cr/Cr:Ni thermocouples as electric leads that were attached to the sample surface by means of colloidal graphite isopropanol suspension. The temperature gradient along the crystal was generated by a resistor on the “hot” side of the crystal. The data were corrected for the thermocouple contribution using a copper wire. Data acquisition was controlled by custom written software.

Hall-effect measurements were performed at room temperature on a 4-probe sample holder placed between the plates of an electromagnet. The magnetic field was varied in the 0.5−1.25 T range. A Keithley 6220 current source was used to excite the sample, and the Hall voltages were recorded on a Keithley 2182A nanovoltometer. Data acquisition was controlled by custom written software.

Single Crystal X-ray Diffraction Studies. Single-crystal X-ray diffraction experiments were performed using either a STOE IPDS II or IPDS 2T diffractometer using Mo Kα radiation (λ = 0.71073 Å) and operating at 50 kV and 40 mA. Integration and numerical absorption corrections were performed using the X-AREA, X-RED, and X-SHAPE programs. All structure were solved by direct methods and refined by full-matrix least-squares on F^2 using the SHELXTL program package.[24] The TwinRotMat, Rotax, and other PLATON functions[25] of the WinGX platform[26] were used to identify the twinning domains and the correct space group, respectively, for the low temperature crystal structures. The JANA2006[27] software was employed for the refinement of the multiple twinning domains present at low temperature structures. The ISOTROPY[27,28] software was used to calculate the group-subgroup relationships of the perovskite structures and to find the correct space group.

RESULTS AND DISCUSSION

Synthetic Aspects. The synthesis of the materials can be accomplished using a variety of approaches. This includes “crude” methods such as direct mortar and pestle grinding of starting materials at room temperature in air, high temperature fusion of the precursors in silica tubes, and solution growth of single crystals. All methods produce the title compounds, though the purity and properties of the resulting materials vary significantly with the method of synthesis. The previously studied $CsMI_3$ analogues[2c,12] were also prepared and used as reference materials for comparison with the AMI_3 systems.

The materials obtained from the grinding method (see Supporting Information) usually are a mixture of products, the main phase (visually homogeneous black solid) being the desired perovskite, with significant amounts of unreacted precursors as evidenced by the X-ray powder patterns of the solids. This method is fast an efficient and is the method of choice to observe the unusual optical properties of each compound. The solids obtained through this method consistently produce the most intense room temperature PL signal, presumably due to the large degree of defects present or due to interface effects (vide infra).

Another method that gives the perovskite phases quickly is by heating the starting materials together at ~350 °C in air or under a gentle flow of nitrogen. A pure black melt is obtained in all cases after 0.5−1 min and on solidification produces a shiny black material. It is imperative to keep the reaction time short to prevent the volatilization CH_3NH_3I and SnI_4. The latter can be seen on the cooler parts of the tube as an orange liquid. $HC(NH_2)_2I$ also decomposes at that temperature to the volatile *sym*-triazine and NH_4I.[29] The materials prepared in this fashion are obtained in higher yield compared to the ones prepared at room temperature by grinding, but the presence of oxidation products (i.e., SnI_4) and the loss of some of the organic cation render these materials defective, not following the exact stoichiometry. The presence of oxidized impurities is evident by thermogravimetric analysis (to be discussed in detail later) by following the mass loss anomalies in the 150−200 °C, where SnI_4 is expected to melt and volatilize. For comparison, the Pb compounds do not show any mass loss in this region (PbI_4 is not known). Instead, the oxidation mechanism on prolonged heating for the Pb solids (in air) produces purple vapor of I_2 with subsequent formation of PbO in the solid state.

Using solid state reactions we were able to isolate the materials in pure form by grinding the precursors together, followed by subsequent annealing at 200 °C inside vacuum-sealed pyrex tubes for ~2 h. Again, some condensation was seen on the cooler parts of the tube (mainly formation of the white organic iodide salt and/or orange SnI_4 crystals in Sn-containing compounds at the sand bath-air interface). Therefore, the materials prepared by this method are stoichiometrically defective as well, but contain no oxidation byproducts compared to those from the open tube methods.

The method of choice to obtain pure materials with exact stoichiometries and lowest number of defects is the solution method. Through this route we were able to obtain high quality single crystals that allowed X-ray crystal structure characterization. Our synthetic procedure is a modification on a reported method[18] and gives no observable impurities while it allows for easier manipulation of the materials. The crystals of the obtained materials have a well-defined habit which can even be modified depending on the temperature profile of the precipitation. Namely, the products vary from polycrystalline aggregates when precipitation starts at elevated temperatures (ca. 130 °C) under vigorous stirring to discrete polyhedral crystals when crystallization occurs by cooling slowly to room temperature. The crystals have a strong tendency toward a rhombic dodecahedral geometry in general, though each phase adopts a unique habit; thus, **1** and **3** adopt the *elongated* rhombic dodecahedron (rhombo-hexagonal dodecahedron) shape, **2** adopts a more *regular* rhombic dodecahedron, while **4a** adopts the hexagonal prism shape. The crystal habit is clearly reflected on the crystal structure of the solids (Figure 1). Additional examples are given in Supporting Information, Figure S1.

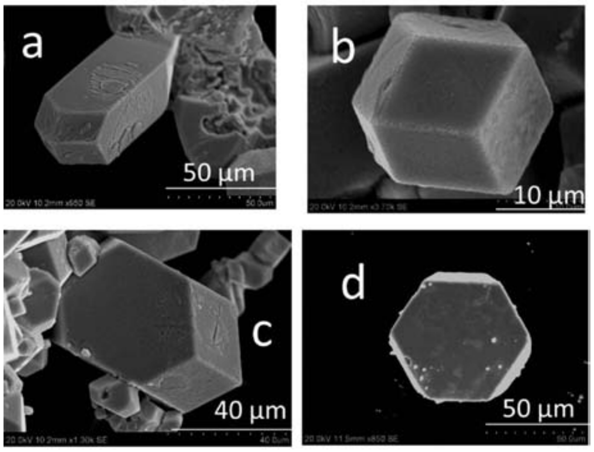

Figure 1. Typical SEM images of **1**−**4** showing the crystal habits of the respective compounds, obtained from the solution method. (a) $CH_3NH_3SnI_3$ (**1**), (b) $HC(NH_2)_2SnI_3$ (**2**), (c) $CH_3NH_3PbI_3$ (**3**), (d) $HC(NH_2)_2PbI_3$ (**4a**).

The materials obtained from the aqueous HI/H_3PO_2 solution mixture are exceptionally pure as judged by X-ray diffraction (XRD) (Figure 2 and Supporting Information, Figures S2−S4). This is mainly attributed to the reducing nature of phosphinic acid which is sufficient to suppress any oxidation occurring by reducing I_3^- (formed by aerial oxidation of the solution) back to I^-. This is evident from the disappearance of the dark red color of the triiodide ion from solution (when oxidation occurs) which turns bright yellow when treated with phosphinic acid. The purging effects of phosphinic acid ensure that no stray oxidation products are present during precipitation, while no traceable byproducts were found as a result of the presence of H_3PO_2/H_3PO_3 in the reaction. In most cases the sole product of the reaction was a pure black crystalline phase. Interestingly, in the case of $HC(NH_2)_2PbI_3$ we were able to isolate two isomers; a black cubic perovskite phase (**4a**) and a yellow hexagonal perovskite

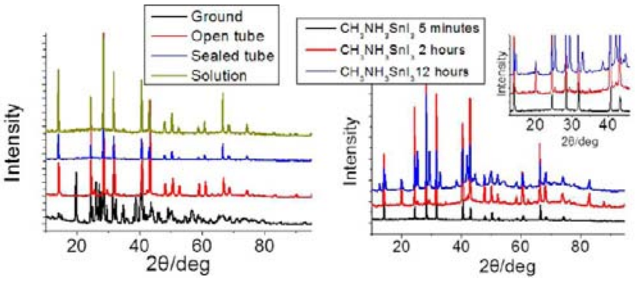

Figure 2. (a) X-ray diffraction patterns of samples of $CH_3NH_3SnI_3$ as functions of the preparative method. (b) X-ray diffraction patterns showing the structural evolution of $CH_3NH_3SnI_3$ standing in moist air over time. The extra peaks that appear most likely belong to the $(CH_3NH_3)_2SnI_6$ compound, as judged indirectly by comparison with the simulated pattern of cubic Cs_2SnI_6 ($Fm\bar{3}m$) which is expected to have a similar structure. The effect is more pronounced following the extended exposure of the material to the atmosphere.

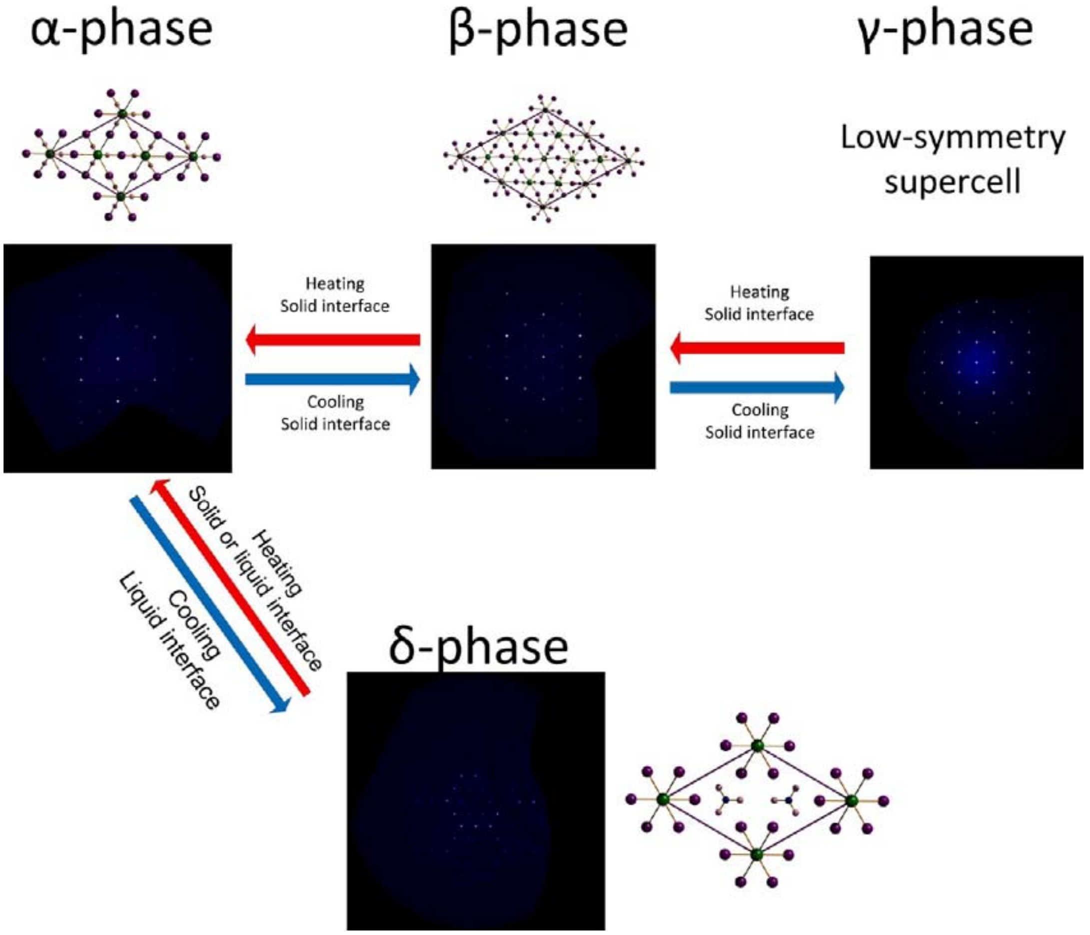

Figure 3. Graphical scheme of the observed phase transitions in the Pb and Sn hybrid perovskites using compound **4** as a representative example. Starting from the *α*-phase two possibilities arise: In the presence of a liquid interface (i.e. inside the mother liquor) it converts to the *δ*-phase upon decreasing the temperature (below 360 K). When dry crystals of the *α*-phase are cooled, however, a different sequence of phase transitions occur with conversion to the *β*- (below~ 200 K) and *γ*- (below ~130 K) phases. Precession images are drawn at [006] view.

phase (**4b**) having a different crystal structure. It appears that the black phase **4a** is stable at high temperatures (>60 °C) while at lower temperatures the black phase fully converts to yellow phases *inside the mother liquor*. When the products are separated from the solvent and dried they interconvert only slowly.

A complication that occurs when trying to isolate pure **4a** is the partial decomposition of formamidine to ammonia and *sym*-triazine in the strongly acidic reaction media using a prolonged reaction time.[29] Whereas the *sym*-triazine does not interfere in the reaction, the ammonium cation slightly complicates the reaction. $NH_4PbI_3{\cdot}2H_2O$,[30] occurring as pale yellow needles, or,[31] as yellow needles, can be detected in **4** as an impurity. The effect can be minimized by keeping the reaction time as short as possible and by avoiding temperatures >150 °C.

It is important to point out that in the case of the Cs analogues $CsSnI_3$ and $CsPbI_3$ the solution method cannot be employed for the preparation of the black forms of these phases, and the yellow phases are isolated instead. The yellow modifications of $CsSnI_3$ (**6a**),[21,12] $CsPbI_3$ (**7**),[2c] are isostructural and crystallize in long, thin, needle-shaped crystals, in accordance with the 1D structure of these materials. The solution method is also capable of producing the black Cs_2SnI_6 phase[5b] (**6b**), an oxidized byproduct in the synthesis of $CsSnI_3$ with a molecular salt structure.

The stability of the materials in air varies. The Pb-containing phases are stable in air for months, though they are affected by humidity and lose their crystalline luster after a couple of weeks. However, this is only a surface effect since the bulk properties of the materials are retained. The Sn-containing materials are air and moisture sensitive and partially decompose within 2 h before total decomposition after 1 d. This behavior is detected in the powder diffraction pattern evolution over time (Figure 2b). The patterns show the appearance of extra Bragg diffraction peaks that belong to the oxidized Sn^{IV} species $(CH_3NH_3)_2SnI_6$, as judged by comparing the diffraction pattern of the unindexed peaks with those of Cs_2SnI_6. A general trend observed is that methylammonium-containing materials are considerably more stable than formamidinium-containing ones. This reflects the respective stability of the cations themselves and particularly the tendency of $HC(NH_2)_2^+$ to dissociate to ammonia and *sym*-triazine.[29]

Structure Description. Single crystals of the materials obtained from the solution method were analyzed by single crystal X-ray diffraction studies. The diffraction measurements were performed at room temperature, and in the range 100–400 K to determine the structural changes that occur during the several phase transitions. The presence of phase transitions is consistent with the perovskite nature of the materials.[1] The common trend for **1**–**4** is that there are two phase transitions that take place leading to three distinct structural modifications.

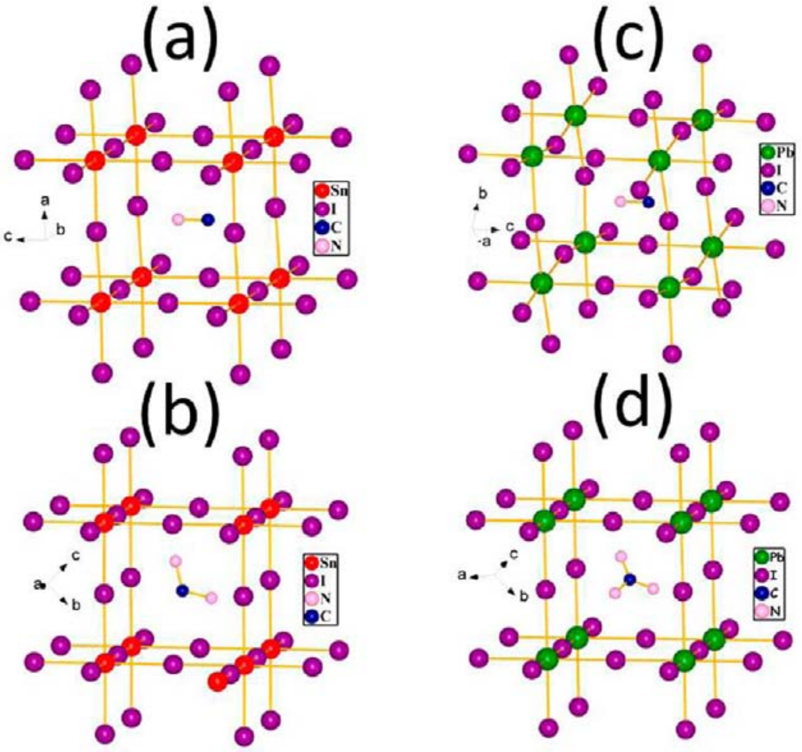

Figure 4. Perovskite building block of (**a**) α-$CH_3NH_3SnI_3$, (**b**) α-$HC(NH_2)_2SnI_3$, (**c**) β-$CH_3NH_3PbI_3$, (**d**) α-$HC(NH_2)_2PbI_3$. Color code: I = purple, Sn = red, Pb = green, C = deep blue, N = pink.

These are classified as the high temperature α-phase, the intermediate temperature β-phase, and the low temperature γ-phase while the nonperovskite yellow phase is termed the δ-phase for consistency with the nomenclature used in the studies of $CsSnI_3$.[2f,g,12] The δ-phase denotes a 1D array of octahedra, and it occurs in δ-$HC(NH_2)_2PbI_3$ (4**b**). A graphical scheme of the phase transitions are summarized in Figure 3.

α-Phase Structures. The α-phase for **1** and **2** is found at room temperature and consists of pseudocubic unit cell with lattice parameter being $a = 6.2307(10)$ Å and $a = 6.3290(9)$ Å, respectively. The α-phase for **3** is also pseudocubic and forms after a phase transition that occurs at temperature >50 °C[42] with lattice parameter $a = 6.3130(2)$ Å. Compound **4a** is unique in adopting a trigonal phase with $a = 8.9817(13)$ Å and $c = 11.0060(20)$ Å at room temperature. We are as yet uncertain if this is the α-phase for **4**a or if there is yet another higher symmetry phase at higher temperatures. For simplicity, here we refer to **4**a as the α-phase. The room temperature structures of **1**−**4** are shown in Figure 4 while the detailed crystallographic information is presented in the Supporting Information.

Because phase transitions affect the PL properties of $CsSnI_3$ (which adopts the orthorhombic γ-phase at room temperature),[19] we decided to investigate the phase transitions that occur in the present hybrid perovskites at different temperatures. A valuable guide was the recent group-theoretical work on perovskite structures.[32] The main difference between $CsMI_3$ inorganic perovskites and the organic hybrid perovskites is the possibility of obtaining the ideal cubic $Pm\bar{3}m$ structure. Whereas in the case of Cs^+ a single atom occupies the 1b Wyckoff position in the center of the cube of the perovskite structure in a primitive unit cell, in the cases of $CH_3NH_3^+$ and $HC(NH_2)_2^+$ this is not possible in this space group. As a consequence, these cations tend to be disordered in the cage. In a cubic unit cell this requires one atom to be placed exactly on the special position and the other(s) to be disordered around the 12 possible orientations inside the cube. Such a situation is not particularly appealing on chemical grounds, especially so if one considers the hydrogen bonding capabilities of both $CH_3NH_3^+$ and $HC(NH_2)_2^+$. Moreover, when a polar organic cation is confined inside the cage its dipole moment cannot be canceled out, thus inducing noncentrosymmetric domains in the crystal.

With this in mind, in our consideration of the crystal structure determinations when an ambiguity occurs we prefer the noncentrosymmetric space group as the correct choice. Of course, when supercells arise from the phase transition an inversion center might emerge which will cancel the dipole moments. At room temperature, the crystal structures of **1**−**4** are noncentrosymmetric. The observed space groups (except for β-$CH_3NH_3PbI_3$ which already has a supercell at this temperature) are classified into the "ferroelectric distortion" category, which means that they are subgroups of the ideal $Pm\bar{3}m$ space group by abolishing certain symmetry elements including the center of symmetry. In this case the symmetry elements are lost as a result of the displacement of the *B* cation from the center of the octahedron, though the ferroelectric displacement is only marginal (0.08 Å along *c*-axis for **1**, 0.05 Å along *b* and *c* axes for **2**, 0.05 Å along *c*-axis for **3** and ~0.004 Å for along *c*-axis for **4a** from the ideal position). In *P*4*mm*, which is adopted by the higher temperature phase of $CH_3NH_3SnI_3$ (**1**) and $CH_3NH_3PbI_3$ (**3**), the displacement occurs along the tetragonal *c*-axis while in *Amm*2, the space group adopted by $HC(NH_2)_2SnI_3$ (**2**) at high temperature, the M atom displacement occurs along the *a and b* axes.

α-$HC(NH_2)_2PbI_3$ (**4a**) is a special case because its space group (centrosymmetric $P\bar{3}m1$) seems to be the parent phase for the family of perovskites termed "1:2 B cation ordering".[32b] The peculiarity arises from the fact that there is only one type of B-cation -Pb- and the reason behind this ordering presently is not understood. Following this distortion, there are three crystallographically inequivalent Pb cations inside the unit cell. In Figure 5 the symmetry elements of the space groups are highlighted with respect to the ideal parent structure.

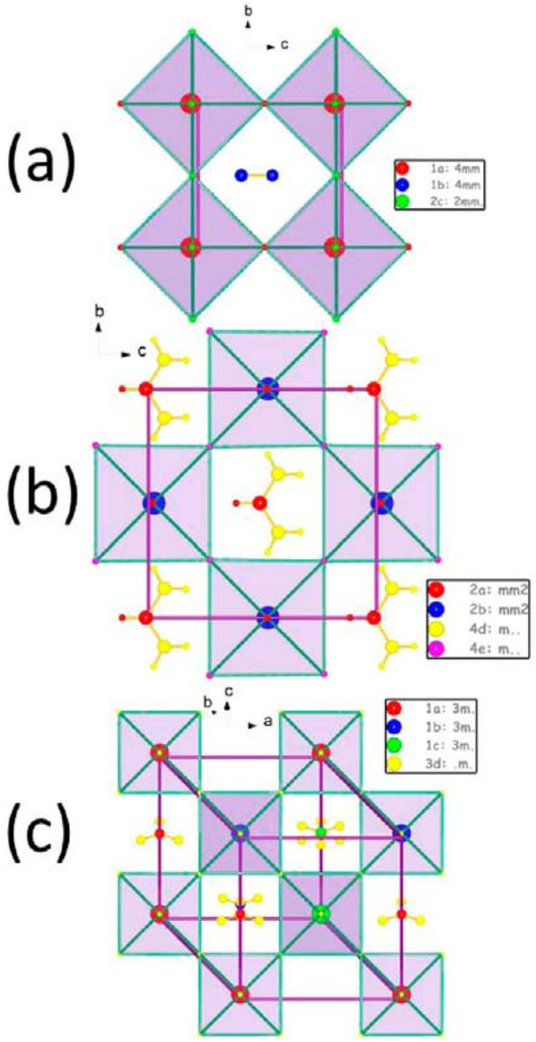

Figure 5. Unit cells of (a) the α-phases of $CH_3NH_3SnI_3$ and $CH_3NH_3PbI_3$ (001 view), (b) $HC(NH_2)_2SnI_3$ (001 view), and (c) $HC(NH_2)_2PbI_3$ (0$\bar{1}$1 view) and demonstrating slight and strong off-centering distortions in the octahedra. Color labeling is according to the Wyckoff positions of each space group.

$CH_3NH_3PbI_3$ adopts the β-phase at room temperature which is distorted (vide infra), and for this reason we sought to solve the structure of the α-phase using the same specimen by raising the temperature above the reported transition at ~330 K.[20a,c] We solved the crystal structure of α-$CH_3NH_3PbI_3$ by measuring a crystal at 400 K and found it to be isostructural to α-$CH_3NH_3SnI_3$. For the collection of good X-ray diffraction data sets we found it essential for the crystal to be maintained at the collection temperature for at least 2 h (to complete the phase transition) before starting the data collection.

β-Phase Structures. Attempts to determine the crystal structures of the hybrid AMI_3 materials revealed the second major well-known property of perovskites, namely, multiple twinning on lowering of crystallographic symmetry.[33] This happens when moving from high to low symmetry distorting the unit cell. For the crystal to comply with such a distortion it "splits" into several domains, a fact that certainly complicates the structure determination. All typical pseudomerohedral twin domains characteristic of the perovskite structure were observed during structure refinement, along the [010], [101], and [121] lattice directions.[1] In all cases the effect was *fully reversible* and when the temperature was raised the crystal was completely reassembled. Another interesting point here is that when we move from the low to the higher symmetry phase during a phase transition, this effect is not so severe, as it was observed, for example, in the case of $CH_3NH_3PbI_3$. Effectively, this behavior suggests that the transition is smoother on lowering the symmetry and more abrupt when increasing it, a trend that is confirmed by the charge transport measurements (vide infra).

The temperature range where the α-phase converts to the β-phase lies between 300 and 150 K for the hybrid perovskites, with the exception of $CH_3NH_3PbI_3$ where the transition takes place at 333 K. Lowering of the symmetry is achieved by means of tilting of the octahedra. Pure octahedral tilting starting from an ideal cubic $Pm\bar{3}m$ structure follows a specific sequence of descending symmetry leading to a certain set of possible space groups. Such a situation is described using the Glazer notation.[34] This notation describes the distortion about *a*, *b*, *c* axes using the axis symbol accompanied by a "+" or "−" symbol to denote if the tilting between two adjacent polyhedral is in-phase or out-of-phase, respectively. Following the space group sequence for $CsSnI_3$, starting with the ideal $Pm\bar{3}m$ structure, it follows a phase transition at ~425 K to the tetragonal structure, $P4/mbm$ (double cell volume), before obtaining an orthorhombic structure, *Pnma* (quadruple cell volume) below 351 K. Such a sequence can be described by considering a pure perovskite tilting model, ignoring ferroelectric-type displacements, with an in-phase distortion along *c*-axis initially and distortions along the *a*- and *b*-axes in the orthorhombic phase. The situation for the hybrid perovskites appears to be different because both ferroelectric and tilting distortions should be taken into consideration. Crystallographic data for the α- and β-phases of **1**−**4** are given in Tables 1 and 2. Table 3 summarizes the crystallographic data for the related compounds **4b**, **5b**, **6b**, and **7**. Atomic coordinates can be found in the Supporting Information, Tables S1−S24.

Both $CH_3NH_3SnI_3$ and $CH_3NH_3PbI_3$ distort in a similar manner in their β-phase, showing out-of-phase tilting of the polyhedra combined with ferroelectric type of off-centering along the *c*-axis adopting the tetragonal *I*4*cm* space group (Figure 5). The ferroelectric displacement component is once again microscopic effecting a slight polarization of the octahedra along the *c*-axis. The tilting angle is 17.4° and 16.4° for $CH_3NH_3SnI_3$ and $CH_3NH_3PbI_3$ as measured at 150 K and 293 K, respectively. At 180 K the framework of $HC(NH_2)_2SnI_3$ is found to be orthorhombic *Imm*2. The onset of the transition is at approximately 250 K. It displays two major distortions at 9.7° and 11.2° and a minor one at 2.2°. $HC(NH_2)_2PbI_3$ at 150 K adopts the *P*3 trigonal space group following a quadrupling of the room temperature cell volume. There is a broad array of distortions, due to significant off-centering of Pb, roughly averaged between the values of 9.0°

Table 1. Crystallographic Data of the α-Phases for 1−4[a]

	α-$CH_3NH_3SnI_3$ (**1**)	α-$HC(NH_2)_2SnI_3$ (**2**)	α-$CH_3NH_3PbI_3$ (**3**)	α-$HC(NH_2)_2PbI_3$ (**4a**)
temperature	293(2) K	340(2) K	400(2) K	293(2) K
crystal system	tetragonal	orthorhombic	tetragonal	trigonal
space group	*P*4*mm*	*Amm*2	*P*4*mm*	*P*3*m*1
unit cell dimensions	a = 6.2302(10) Å, α = 90.00°	a = 6.3286(10) Å, α = 90.00°	a = 6.3115(2) Å, α = 90.00°	a = 8.9817(13) Å, α = 90.00°
	b = 6.2302(10) Å, β = 90.00°	b = 8.9554(11) Å, β = 90.00°	b = 6.3115(2) Å, β = 90.00°	b = 8.9817(13) Å, β = 90.00°
	c = 6.2316(11) Å, γ = 90.00°	c = 8.9463(11) Å, γ = 90.00°	c = 6.3161(2) Å, γ = 90.00°	c = 11.006(2) Å, γ = 120.00°
volume	241.88(7) $Å^3$	507.03(12) $Å^3$	251.60(2) $Å^3$	768.9(2) $Å^3$
Z	1	2	1	3
density (calculated)	3.649 g/cm^3	3.566 g/cm^3	4.092 g/cm^3	4.101 g/cm^3
absorption coefficient	12.128 mm^{-1}	11.579 mm^{-1}	25.884 mm^{-1}	25.417 mm^{-1}
F(000)	228	468	260	798
crystal size (mm^{-3})	0.053 × 0.032 × 0.021	0.176 × 0.163 × 0.136	0.035 × 0.022 × 0.017	0.041 × 0.026 × 0.021
θ range	3.27 to 28.94°	3.22 to 29.11°	3.23 to 24.92°	1.85 to 29.19°
index ranges	$-8 \leq h \leq 8$,	$-8 \leq h \leq 8$,	$-7 \leq h \leq 7$,	$-12 \leq h \leq 12$,
	$-8 \leq k \leq 8$,	$-10 \leq k \leq 12$,	$-6 \leq k \leq 6$,	$-12 \leq k \leq 11$,
	$-8 \leq l \leq 8$	$-12 \leq l \leq 10$	$-7 \leq l \leq 7$	$-15 \leq l \leq 15$
reflections collected	2164	2490	1628	7475
independent reflections	411 [R_{int} = 0.0458]	686 [R_{int} = 0.0517]	300 [R_{int} = 0.0700]	1645 [R_{int} = 0.0459]
completeness to θ	θ = 28.94°, 98.2%	θ = 29.11°, 100%	θ = 24.92°, 98.2%	θ = 29.19°, 99.6%
data/restr./param.	411/2/16	686/3/24	300/2/19	1645/7/44
goodness-of-fit	1.262	0.861	1.176	0.908
final R indices [>2σ(I)]	R_{obs} = 0.0327,	R_{obs} = 0.0323,	R_{obs} = 0.0417,	R_{obs} = 0.0398,
	wR_{obs} = 0.0576	wR_{obs} = 0.0577	wR_{obs} = 0.0981	wR_{obs} = 0.0666
R indices [all data]	R_{all} = 0.0451,	R_{all} = 0.0615,	R_{all} = 0.0417,	R_{all} = 0.0892,
	wR_{all} = 0.0613	wR_{all} = 0.0632	wR_{all} = 0.0981	wR_{all} = 0.0807
2nd twin domain	[−1 0 0 0 0 1 0 1 0]49(69) %	[0 $-^1/_2$ $-^1/_2$ −1 $-^1/_2$ $^1/_2$ −1 $^1/_2$ $-^1/_2$] 43(3) %	[−1 0 0 0 0 1 0 1 0] 36(3) %	[−1 0 0 0 −1 0 0 0 1] 6.36(2) %
Flack parameter	[−1 0 0 0 −1 0 0 0 −1] −4(45) %	[−1 0 0 0 −1 0 0 0 −1] −50(32) %	[−1 0 0 0 −1 0 0 0 −1] 12(3) %	[−1 0 0 0 −1 0 0 0 −1] 20(15) %
2nd domain Flack parameter	[1 0 0 0 0 1 0 1 0] 3(68) %	[0 $-^1/_2$ $-^1/_2$ −1 $^1/_2$ $^1/_2$ −1 $^1/_2$ $^1/_2$] 13(3) %	[1 0 0 0 0 1 0 1 0] 37(4) %	not refined
extinction coefficient		0.0200(4)	0.016(2)	
largest diff. peak/hole	0.895/−0.861 e·$Å^{-3}$	0.394/−0.952 e·$Å^{-3}$	1.871/−2.008 e·$Å^{-3}$	1.104/−1.727 e·$Å^{-3}$
wavelength	0.71073 Å			
refinement method	full-matrix least-squares on F^2			

[a] $R = \sum||F_o| - |F_c||/\sum|F_o|$, $wR = \{\sum[w(|F_o|^{22} - |F_c|^2)^2]/\sum[w(|F_o|^{44})]\}^{1/2}$ and calc $w = 1/[\sigma^2(F_o^2) + (0.0262P)^2 + 0.0000P]$ where $P = (F_o^2 + 2F_c^2)/3$.

and 11.5°. For good measure, the 373 K distortion of β-$CsSnI_3$ is 18.4°.

From Figure 6 it is apparent that the methylammonium compounds have a tendency to distort the octahedra in the out-of-phase mode, whereas formamidinium phases seem to distort in-phase, the latter being similar to β-$CsSnI_3$. Contrary to the purely inorganic phase, however, the distortions lead to lower symmetry of the lattice whence the tilting of the octahedra is less severe.

γ-Phase Structures. As the temperature continues to decrease further symmetry lowering occurs leading to the γ-phases. The γ-phase is encountered close to 100 K, but for γ-$CH_3NH_3PbI_3$ this temperature was found to be at ~150 K. The γ-phases are easily recognizable from diffraction studies because of an intense broadening and splitting of the Bragg peaks in addition to the extra spots that appear. This can be clearly seen in the precession images generated from diffraction data collected at 100 K (Supporting Information, Figure S5), as compared to those created from room temperature data (Supporting Information, Figure S6). We were unable to refine the structure of the γ-phases mostly because about 50% of the observed peaks remain unindexed during the unit cell determination. The unindexed peaks result from the formation of multiple twin domains which are created by the "freezing" of

Table 2. Crystallographic Data of the β-phases for 1–4[a]

	β-$CH_3NH_3SnI_3$ (1)	β-$HC(NH_2)_2SnI_3$ (2)	β-$CH_3NH_3PbI_3$ (3)	β-$HC(NH_2)_2PbI_3$ (4a)
temperature	200(2) K	180(2) K	293(2) K	150(2) K
crystal system	tetragonal	orthorhombic	tetragonal	trigonal
space group	*I4cm*	*Imm2*	*I4cm*	*P3*
unit cell dimensions	a = 8.7577(15) Å, α = 90.00° b = 8.7577(15) Å, β = 90.00° c = 12.429(3) Å, γ = 90.00°	a = 12.5121(9) Å, α = 90.00° b = 12.5171(8) Å, β = 90.00° c = 12.5099(9) Å, γ = 90.00°	a = 8.849(2) Å, α = 90.00° b = 8.849(2) Å, β = 90.00° c = 12.642(2) Å, γ = 90.00°	a = 17.7914(8) Å, α = 90.00° b = 17.7914(8) Å, β = 90.00° c = 10.9016(6) Å, γ = 120.00°
volume	953.2(3) $Å^3$	1959.2(2) $Å^3$	990.0(4) $Å^3$	2988.4(3) $Å^3$
Z	4	8	4	12
density (calculated)	3.703 g/cm^3	3.692 g/cm^3	4.159 g/cm^3	4.221 g/cm^3
absorption coefficient	12.309 mm^{-1}	11.986 mm^{-1}	26.312 mm^{-1}	26.159 mm^{-1}
$F(000)$	912	1872	1040	3192
crystal size (mm^{-3})	0.158 × 0.111 × 0.089	0.018 × 0.014 × 0.009	0.005 × 0.003 × 0.002	0.038 × 0.030 × 0.023
θ range	4.65 to 24.94°	2.30 to 29.15°	3.26 to 29.03°	1.87 to 25.00°
index ranges	$-9 \leq h \leq 10$, $-10 \leq k \leq 9$, $-14 \leq l \leq 14$	$-17 \leq h \leq 17$, $-17 \leq k \leq 17$, $-17 \leq l \leq 17$	$-12 \leq h \leq 12$, $-12 \leq k \leq 10$, $-16 \leq l \leq 15$	$-21 \leq h \leq 20$, $-21 \leq k \leq 21$, $-12 \leq l \leq 12$
reflections collected	3058	9462	4483	19512
independent reflections	521 [R_{int} = 0.1007]	2876 [R_{int} = 0.0464]	678 [R_{int} = 0.0664]	7026 [R_{int} = 0.0596]
completeness to θ	θ = 24.94°, 99.2%	θ = 29.15°, 99.7%	θ = 29.03°, 97.1%	θ = 25.00°, 100%
data/restr./param.	521/2/21	2876/1/47	678/2/18	7026/18/192
goodness-of-fit	1.142	0.963	1.268	0.839
final R indices [$>2\sigma(I)$]	R_{obs} = 0.0637, wR_{obs} = 0.1442	R_{obs} = 0.0486, wR_{obs} = 0.1276	R_{obs} = 0.0378, wR_{obs} = 0.0865	R_{obs} = 0.0656, wR_{obs} = 0.1584
R indices [all data]	R_{all} = 0.0639, wR_{all} = 0.1443	R_{all} = 0.0780, wR_{all} = 0.1432	R_{all} = 0.0418, wR_{all} = 0.0879	R_{all} = 0.1780, wR_{all} = 0.2133
2nd twin domain	[$-^1/_2$ $^1/_2$ $^1/_2$ $^1/_2$ $-^1/_2$ $^1/_2$ 1 1 0] 7.9(2) %	[0 0 −1 0 −1 0 −1 0 0] 19.74(6) %	[−1 0 0 0 1 0 0 0 −1] 50(4) %	[−1 0 0 0 −1 0 0 0 1] 94.19(2) %
Flack parameter	[−1 0 0 0 −1 0 0 0 −1] −34(23) %	[−1 0 0 0 −1 0 0 0 −1] 9(5) %	[−1 0 0 0 −1 0 0 0 −1] 0(10) %	[−1 0 0 0 −1 0 0 0 −1] 51(5) %
2nd domain Flack parameter	[$^1/_2$ $^1/_2$ $^1/_2$ $^1/_2$ $^1/_2$ $^1/_2$ 1 1 0] 16.7(2) %	[0 0 −1 0 1 0 −1 0 0] 23.78(6) %	not refined	not refined
extinction coefficient	0.00247(6)	0.000808(18)		0.000498(8)
largest diff. peak/hole	2.002/−1.194 $e \cdot Å^{-3}$	2.606/−1.191 $e \cdot Å^{-3}$	0.927/−1.676 $e \cdot Å^{-3}$	3.391/−4.496 $e \cdot Å^{-3}$
wavelength	0.71073 Å			
refinement method	full-matrix least-squares on F^2			

[a] $R = \sum||F_o| - |F_c||/\sum|F_o|$, $wR = \{\sum[w(|F_o|^{22} - |F_c|^2)^2]/\sum[w(|F_o|^{44})]\}^{1/2}$ and calc $w = 1/[\sigma^2(F_o^2) + (0.0262P)^2 + 0.0000P]$ where $P = (F_o^2 + 2F_c^2)/3$.

the cations (and subsequently the perovskite lattice) in different orientations. From our attempts to solve the crystal structures, we estimate that the γ-phases adopt a monoclinic crystal system. The methylammonium phases of Sn and Pb seem to acquire a *C*-centered cell whereas the formamidinium perovskites seem to adopt a primitive cell. It is however necessary to highlight a distinction between the methylammonium and formamidinium behavior; whereas the γ-phase of the former contains many split peaks, for the latter the splitting is much less intense and instead superlattice ordering is observed leading to multiplication of the parent unit cell. This may be attributed to the point group symmetry of $CH_3NH_3^+$ (C_{3v}) as opposed to that of $HC(NH_2)_2^+$ (C_{2v}), with the latter being more "flexible" to comply with the lattice distortions. The phase transitions of a similar compound, $CH_3NH_3SnBr_3$, have been recently investigated by means of high resolution powder diffraction studies.[35] The authors were able to solve the crystal structure of the β-$CH_3NH_3SnBr_3$ modification, but they too were unable to refine the crystal structure of the γ-phase in a satisfactory manner upon entering into the peak splitting regime. They concluded that the crystal structure may be triclinic based on density function theory (DFT) calculations.

δ-Phase Structures. Interestingly, the δ-phase of $HC(NH_2)_2PbI_3$ (Figure 7) is markedly different from the δ-phase occurring in $CsSnI_3$ and $CsPbI_3$; in the latter case the structure comprises a double chain of MI_6^{4-} octahedra.[2c,36] The intrachain linking of the polyhedra in the individual chains is affected by edge-sharing of square bipyramidal units. The octahedral coordination occurs by interchain bonding by a relatively longer M–I bond with an iodide occupying a basal position of the square pyramid, overall adopting the NH_4CdCl_3-type structure. δ-$HC(NH_2)_2PbI_3$ on the other hand consists of face-sharing octahedra propagating along the 001 direction forming single chains, with the cations occupying the space between the chains, thus adopting a nearly *hcp*-lattice ($P6_3mc$). The deviation from the ideal symmetry can be attributed to the $HC(NH_2)_2^+$ cations which lack a center of inversion despite the fact that the nitrogen atoms where treated as disordered during the structure determination process. At this point we should stress that the black-to-yellow transformation is a reversible effect. For example, when a single crystal of δ-$HC(NH_2)_2PbI_3$ is heated at 400 K for ~2 h a polycrystalline black solid is formed instead, though not in a single-crystal-to single-crystal manner. Interestingly, while the α- to δ-phase transformation can be repeated indefinitely in the

Table 3. Crystallographic Data of the β-phases for 4b, 5b, 6b, and 7^a

	δ-HC(NH$_2$)$_2$PbI$_3$ (**4b**)	β-CH$_3$NH$_3$Sn$_{0.46}$Pb$_{0.54}$I$_3$ (**5b**)	α-Cs$_2$SnI$_6$ (**6b**)	δ-CsPbI$_3$ (**7**)
temperature	293(2) K	293(2) K	293(2 K)	293(2) K
crystal system	hexagonal	tetragonal	cubic	orthorhombic
space group	$P6_3mc$	$I4cm$	$Fm\bar{3}m$	$Pnma$
unit cell dimensions	a = 8.6603(14) Å, α = 90.00°	a = 8.8552(6) Å, α = 90.00°	a = 11.6276(9) Å, α = 90.00°	a = 10.4342(7) Å, α = 90.00°
	b = 8.6603(14) Å, β = 90.00°	b = 8.8552(6) Å, β = 90.00°	b = 11.6276(9) Å, β = 90.00°	b = 4.7905(3) Å, β = 90.00°
	c = 7.9022(6) Å, γ = 120.00°	c = 12.5353(12) Å, γ = 90.00°	c = 11.6276(9) Å, γ = 90.00°	c = 17.7610(10) Å, γ = 90.00°
volume	513.27(12) Å^3	982.95(13) Å^3	1572.1(2) Å^3	887.78(10) Å^3
Z	2	4	4	4
density (calculated)	4.096 g/cm^3	3.870 g/cm^3	4.842 g/cm^3	5.393 g/cm^3
absorption coefficient	25.384 mm^{-1}	19.219 mm^{-1}	17.925 mm^{-1}	33.373 mm^{-1}
F(000)	532	964	1912	1184
crystal size (mm^{-3})	0.062 × 0.046 × 0.031	0.191 × 0.160 × 0.109	0.071 × 0.053 × 0.044	0.265 × 0.022 × 0.013
θ range	2.72 to 24.99°	2.82 to 29.01°	3.03 to 28.96°	2.26 to 29.16°
index ranges	$-10 \leq h \leq 7$,	$-10 \leq h \leq 12$,	$-15 \leq h \leq 15$,	$-14 \leq h \leq 14$,
	$-9 \leq k \leq 10$,	$-11 \leq k \leq 11$,	$-14 \leq k \leq 15$,	$-5 \leq k \leq 6$,
	$-8 \leq l \leq 9$	$-17 \leq l \leq 17$	$-15 \leq l \leq 15$	$-22 \leq l \leq 24$
reflections collected	1687	4728	3871	7985
independent reflections	354 [R_{int} = 0.0759]	788 [R_{int} = 0.0738]	143 [R_{int} = 0.0595]	1330 [R_{int} = 0.0733]
completeness to θ	θ = 24.99°, 100%	θ = 29.01°, 100%	θ = 28.96°, 100%	θ = 29.16°, 99%
data/restr./param.	354/3/17	788/2/22	143/0/7	1330/0/32
goodness-of-fit	1.055	1.162	1.483	1.069
final R indices [>2σ(I)]	R_{obs} = 0.0437,	R_{obs} = 0.0678,	R_{obs} = 0.0317,	R_{obs} = 0.0266,
	wR_{obs} = 0.1066	wR_{obs} = 0.1732	wR_{obs} = 0.0697	wR_{obs} = 0.0457
R indices [all data]	R_{all} = 0.0516,	R_{all} = 0.0809,	R_{all} = 0.0322,	R_{all} = 0.0364,
	wR_{all} = 0.1102	wR_{all} = 0.1809	wR_{all} = 0.0698	wR_{all} = 0.0477
2nd twin domain	[−1 −1 0 0 1 0 0 0 −1] 39(7) %	[$-^1/_2$ $^1/_2$ $-^1/_2$ $^1/_2$ $-^1/_2$ $-^1/_2$ −1 −1 0] 25(1) %		
Flack parameter	[−1 0 0 0 −1 0 0 0 −1] 0(3) %	[−1 0 0 0 −1 0 0 0 −1] 28(5) %		
2nd domain Flack parameter	not refined	[$^1/_2$ $^1/_2$ $-^1/_2$ $^1/_2$ $^1/_2$ $-^1/_2$ −1 −1 0] 22(1) %		
extinction coefficient	0.0081(15)	0.00084(10)	0.00247(12)	0.0127(3)
largest diff. peak/hole	1.975/−0.721 e·Å^{-3}	2.980/−2.175 e·Å^{-3}	1.005/−1.241 e·Å^{-3}	0.887/−1.986 e·Å^{-3}
wavelength	0.71073 Å			
refinement method	full-matrix least-squares on F^2			

^{a}R = $\sum||F_o| - |F_c||/\sum|F_o|$, wR = $\{\sum[w(|F_o|^{22} - |F_c|^2)^2]/\sum[w(|F_o|^{44})]\}^{1/2}$ and calc $w = 1/[\sigma^2(F_o^2) + (0.0262P)^2 + 0.0000P]$ where $P = (F_o^2 + 2F_c^2)/3$.

mother liquor by running heating and cooling cycles in the absence of a liquid medium, the transformation is *irreversible*; that is, the polycrystalline black material of the α-phase obtained from heating a crystal of the δ-phase does not convert back to the yellow phase on cooling or it does so only very slowly. This is likely due to the partial loss of formamidinium resulting in a defective compound.

Thermal Analysis. The thermal analysis results for the hybrid perovskites presented here show similar trends for Sn and Pb. The experiments were conducted under a nitrogen flow to avoid oxidation. Thermogravimetric analysis of the materials shows that they decompose before melting. Decomposition starts at temperatures >300 °C (Figure 8) and proceeds in one step. The mass loss corresponds to loss of the organic cation and all the iodide content leaving a metallic residue.

The decomposition profiles seem to be dependent on the synthetic conditions used to prepare the compounds. When the materials are prepared in air the decomposition follows a different pathway that includes two distinct weight loss steps. In that case, the decomposition proceeds initially with a mass loss corresponding to "CH_3NH_3I" or "HC(NH$_2$)$_2$I", possibly in the form of the free amine and HI, followed by a second step in mass loss corresponding to loss of HI molecules. An example of this is $CH_3NH_3SnI_3$ (**1**), where the mass loss depends on the preparative method employed (Figure 8a). It is clearly seen that the mass loss is associated with the purity of the material. Therefore, it seems unlikely that the first decomposition step is associated with loss of the organic cation alone. For example, when the material is prepared by grinding, the first step of decomposition displays a much greater mass loss as compared to the material prepared by high temperature solid state or solution methods. A plausible explanation for this behavior is the presence of Sn^{4+} species in the compounds. In that case, the mass loss could be associated with the liberation of volatile SnI_4. Contributing to the weight loss is the liberation of CH_3NH_3I (in the form of CH_3NH_2 and HI) which is driven away due to the formation of Sn^{4+} species. It is worth pointing out that the decomposition temperature of CH_3NH_3I is roughly 280 °C, while the decomposition of partly oxidized $CH_3NH_3SnI_3$ (with weight loss) starts at ~150 °C. Further support for the presence of Sn^{4+} species is provided by the absence of a corresponding "two step" decomposition profile in $CH_3NH_3PbI_3$, although a two-step decomposition is indeed observed for the solution prepared sample. In the former case

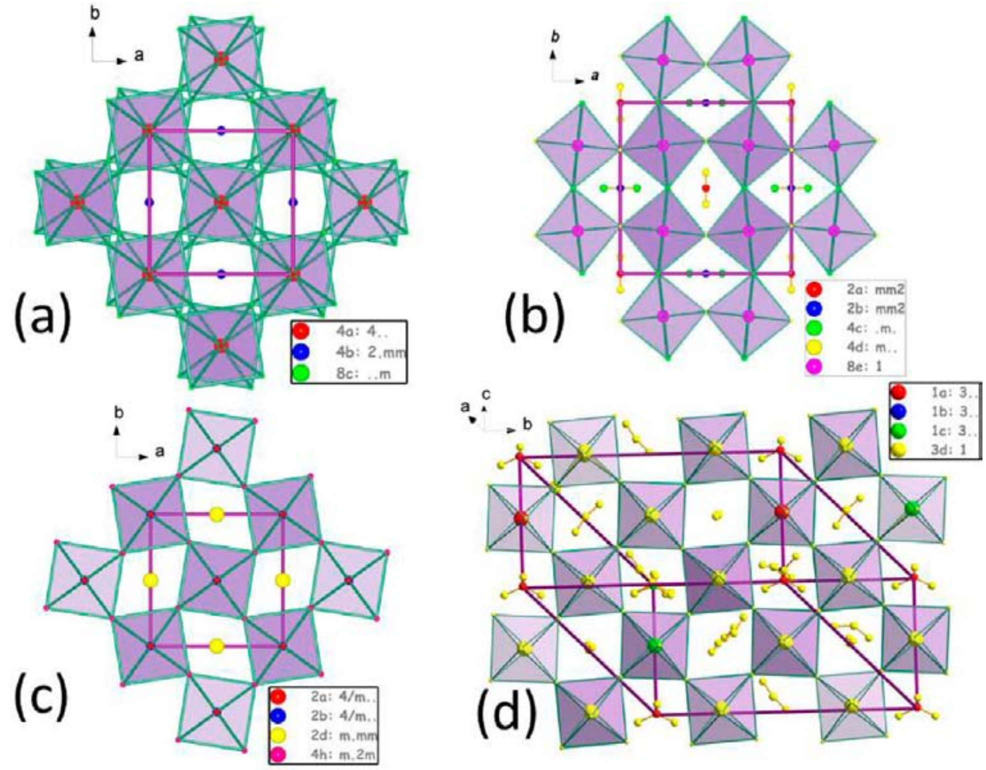

Figure 6. Unit cells of (a) the β-phases of $CH_3NH_3SnI_3$ and $CH_3NH_3PbI_3$ (001 view), (b) $HC(NH_2)_2SnI_3$ (001 view) highlighting the tilting of the octahedra. (c) The unit cell of β-$CsSnI_3$ (ICSD-69995), given here for comparison purposes. (d) The unit cell of $HC(NH_2)_2PbI_3$ ($0\bar{2}1$ view). Color labeling is according to the Wyckoff positions of each space group.

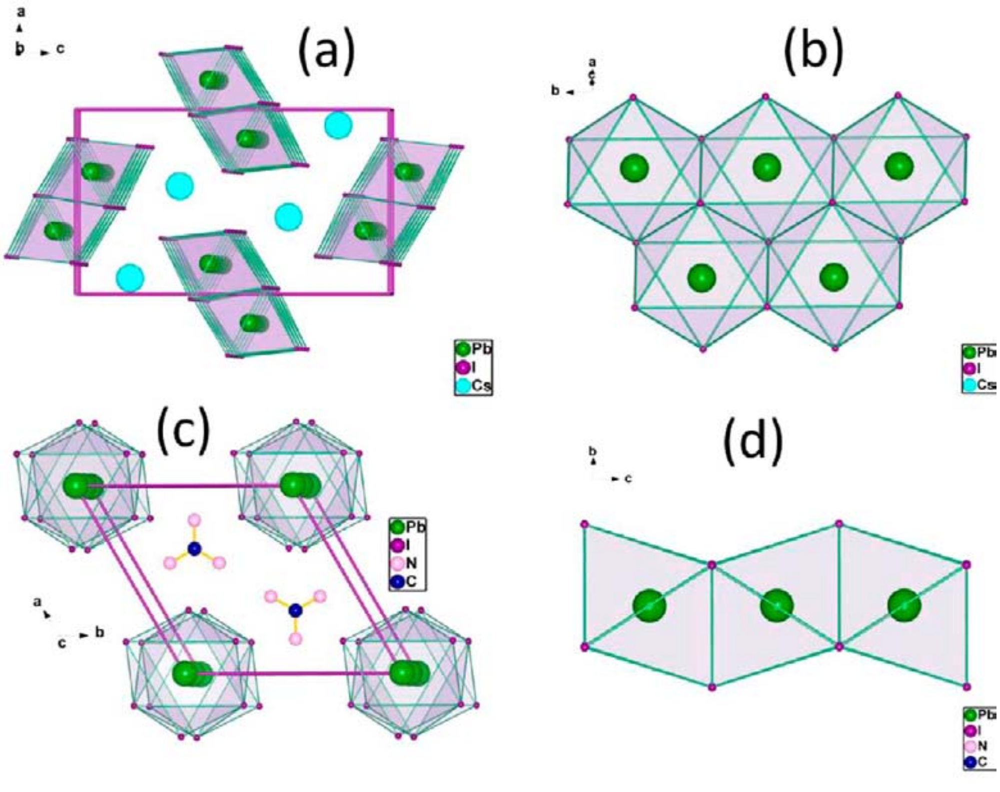

Figure 7. Unit cells of (a) δ-$CsPbI_3$ and (c) δ-$HC(NH_2)_2PbI_3$ viewed along the [010] and [100] directions, respectively. The corresponding building blocks of the 1D chains are shown in (b) and (d). The nitrogen atoms of the formamidinium atoms are disordered down the 3-fold symmetry axis with 2/3 partial occupancy in (c).

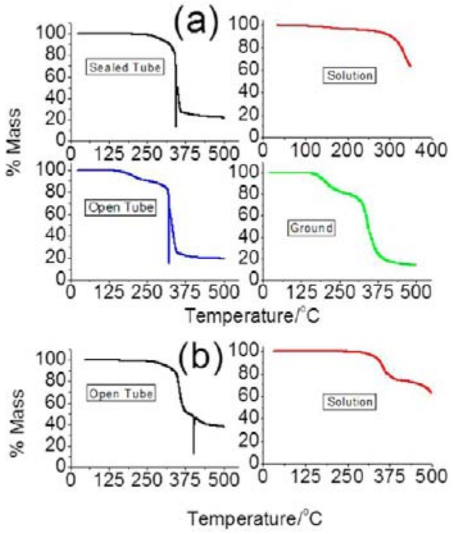

Figure 8. (a) TGA analysis of $CH_3NH_3SnI_3$ as a function of the synthetic route employed. A two-step decomposition process can be seen for the less "pure" phases. (b) TGA analysis of $CH_3NH_3PbI_3$ prepared from the solution and open tube methods showing no changes as a function of the preparative route. The measurements were conducted under a constant flow of nitrogen to avoid oxidation. The spike in the data that appears during the decomposition step is from the abrupt gas evolution which perturbs the solid and momentarily loses contact with the sample holder.

this could be explained by the inability of Pb^{2+} to oxidize to Pb^{4+} in an all iodide environment.

As stated above, $CH_3NH_3PbI_3$ does undergo a structural phase transition going from tetragonal to pseudocubic symmetry between 300 and 400 K as determined by single-crystal diffraction studies. The reason for the absence of any thermal signal for this transition may suggest that the transition is of second order as it has been predicted.[37] The transition itself does not involve chemical bond cleavage/formation; the only real change is associated with lowering of symmetry. Subsequently, the change in the heat capacity of the material, $C = Q/\Delta T$, is expected to be small and explains the lack of signal in DTA and DSC. The transition has been reported to occur at 330 K[20c] though the sensitivity of our experimental setup did not allow us to reproduce this result. Plots of the thermal analysis data are given in Supporting Information, Figure S7.

Nevertheless, the phase transition can be better detected by other techniques that are either (local) symmetry sensitive or detect properties that are affected by symmetry. Such examples involve but are not limited to dielectric constant measurements,[20a,38] ^{127}I NQR,[20b] single-crystal resistivity,[2i] ^{1}H NMR spin−lattice relaxation,[20b,39] X-ray diffraction,[40] and Raman spectroscopy.[41] An excellent discussion on the crystal chemistry of $CH_3NH_3PbI_3$ (**3**) has appeared during the preparation of the present manuscript.[42]

In the case of compounds **3** and **4** a similar behavior can be observed with the addition of a small mass loss associated with the evaporation of formamidine or one of its decomposition products.[25] The case of $HC(NH_2)_2PbI_3$ (**4a**) is significantly more complicated as there is some contamination from phase (**4b**) which is probably responsible for the small exothermic mass loss observed at 270 °C (Supporting Information, Figure S8). A decolorized (pale brown) residue remains, indicating the complete loss of iodine from the solid after the analysis.

Optical Properties. *(a). Electronic Spectroscopy.* All materials display a strong, abrupt absorption in the visible spectral region (Figure 9). The absorption has been attributed to the energy gap between the conduction and the valence band, thus classifying the materials as medium-band gap semiconductors. The Sn and Pb based materials display an optical band gap between 1.2 and 1.6 eV, in good agreement with the black color of the solids.

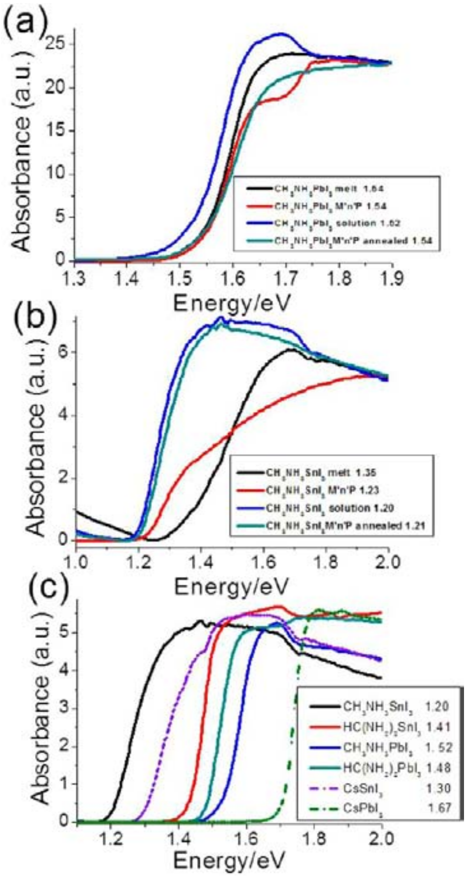

Figure 9. Electronic absorption spectra of **1**−**4**. Panels (a) and (b) highlight the band gap variability on the basis of the synthetic approach employed to prepare the sample. (c) The spectra of specimens of **1**−**4** prepared with the solution method as compared with $CsSnI_3$ and $CsPbI_3$ reference phases (dotted lines) prepared from the open tube method. The value of the band gap is given next to each compound.

The band gaps of the Sn-based perovskites, have mean values between 1.2 and 1.4 with $CH_3NH_3SnI_3$ (**1**) having a consistently smaller band gap with respect to $HC(NH_2)_2SnI_3$ (**2**) for every preparative method employed. We use the term "mean value" because as can be seen in Figure 9 there is a variation of the band gap as a function of the preparative method. There is no obvious trend on this variation besides the interesting fact that $CH_3NH_3SnI_3$ samples prepared in an open tube (1.35 eV), prepared from solution, or in a sealed tube reaction (1.21 eV) show very different properties. This is despite the fact that their thermal behavior is very similar as is their diffraction pattern. When compared with $CsSnI_3$,[12] **1** shows a slight narrowing on the gap whereas **2** shows the opposite trend which is consistent with the lowering in the symmetry of the 3D $[SnI_3]^-$ framework.

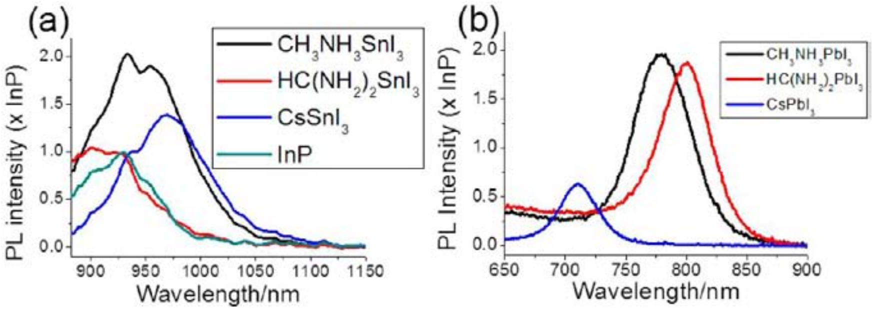

Figure 10. PL spectra of (a) $ASnI_3$ and (b) $APbI_3$ as obtained from the open tube reaction. The data are normalized toward a single crystalline sample of InP which is used as a benchmark. The Cs analogues, prepared in the same manner, are given for comparison purposes.

In contrast to the Sn compounds, the Pb-based phases have band gaps which are independent of the preparation method at 1.45 and 1.52 eV for $HC(NH_2)_2PbI_3$ (**4a**) and $CH_3NH_3PbI_3$ (**3**), respectively. Similar to the Sn-phases, a narrowing of the band gap is observed for the Pb compounds upon symmetry lowering, when compared to the room temperature absorption of the black perovskite form of $CsPbI_3$[24] obtained by a solid state reaction, before the material transitions to the yellow nonperovskitic phase (Figure 9c). The absorption edge for both the Sn- and Pb-based phases is sharp, suggesting a direct band gap. This has been confirmed by theoretical calculations, where all electronic structure models reported predict a direct band gap for the Sn- and Pb-analogues.[12,43]

Overall, the iodide perovskite materials absorb in the spectral region between 1.2 and 1.7 eV. Semiconductors with direct energy gaps between 1.0 and 1.5 eV are highly sought after since they are optimal for solar cell applications yielding the maximum theoretical conversion efficiency.[44] Thus, compounds **1−4** and their Cs^+ analogues having a nearly ideal band gap and favorable charge transport properties (vide infra) are very promising materials for use in high-efficiency solar cells.

(b). PL Properties. The PL properties of specimens obtained from all four synthetic approaches (solution, grinding, open tube melting, sealed tube annealing) were measured at room temperature using a green light source at 532 nm and a specialized PL spectrometer. An intense PL emission was observed for all Sn and Pb compounds. The Pb analogues emit between 700 and 800 nm and the Sn analogues between 850 and 1000 nm, covering a broad region of near-IR spectrum. The emission wavelength is consistent with the experimentally determined band gaps providing further evidence for the direct nature of the band gap.

Compounds that emit in the near-IR region at room temperature are rare, and they are highly sought after for energy conversion applications such as Luminescent Solar Concentrators (LSCs).[45] Currently, the field of LSCs is monopolized by the venerable class of III−V semiconductors with GaAs and InP being the major compounds of interest. We have been using the latter as a benchmark material to evaluate the relative efficiency of **1−4** and to estimate their potential as LSC materials.

The solution-prepared samples showed no PL with the exception of $HC(NH_2)_2PbI_3$, which typically is measured as mixture of the two structural forms (Supporting Information, Figure S9). It is interesting that the materials prepared with any method, other than from solution, are PL-active. Figure 10 shows typical emission spectra of the hybrid perovskites prepared by grinding the precursors and heating the samples at 350 °C for 20 s. Generally, the grinding method consistently produces samples with high PL. Annealing of the ground material also produces solids with respectable luminescence, slightly weaker than the ground ones, but the materials are highly homogeneous. However, we observed that exhaustive annealing, that is, > 24 h, reduces the PL emission (vide infra). When synthesized under vacuum the materials obtained are pure and homogeneous, though the PL-properties are noticeably weakened compared to the samples prepared at ambient pressure. When exposed to the atmosphere, the materials decompose within a few minutes, displaying an extreme sensitivity. The solution-processed solids of both Sn and Pb perovskites are PL-inactive. This suggests that the presence of defects such as Sn^{4+} species in the structure which are more likely to be present in the samples made by solid state methods is probably associated with the PL.

As stated above, there is a significant variation in the optical absorption properties of these materials that depends strongly on the preparation method. Therefore, it is not surprising that the emission properties differ to some extent. The absence of emission from the well-formed solution-grown single crystals of Sn and Pb perovskites is hard to explain. A rough attempt to account for this is to suppose that the materials are relatively PL-inactive in their higher symmetry phase (the α-phase), where the distortions are small. If PL originates from defects it should increase as the symmetry is lowered via twinning, artificially creating defects. The temperature dependence of the PL intensity/wavelength has been confirmed in $CsSnI_3$.[19b] When one of the other three methods (grinding, open tube melting, sealed tube annealing-see Experimental Section) is employed, the resulting polycrystalline materials should have a greater number of defects. We suppose that this might be the source of PL enhancement. Another supporting indication of the defect-induced PL model is that the only solution prepared material that shows some PL-activity is $HC(NH_2)_2PbI_3$ which undergoes a phase transformation from a perovskite structure to a nonperovskite structure incidentally forming a highly defective perovskite phase during transformation. Therefore, the defects likely play a crucial role in the expression of the PL, either when these are created during the synthesis or by means of temperature-controlled structural changes. This is supported by the generally observed trend which is the following: the cruder the synthesis the higher the PL intensity.

In Figure 10, the PL properties of Sn and Pb hybrid materials are presented along with the corresponding Cs phases. The magnitudes of the emission are comparable with one another, except for $CsPbI_3$ in which the perovskite black phase, which is stable above ~300 °C, very rapidly converts to the PL-inactive yellow phase. All samples shown in Figure 10 have been prepared from the melt for the data to be comparable. There is a small but real shift in the emission wavelength which matches well with the corresponding shifts in absorption energy edge.

Charge Transport Properties. Given that the PL properties arise from defects, possibly Sn^{4+} centers acting as dopants in the structure, we performed charge transport measurements on **1**–**3**. The presence of Sn^{4+} could give rise to low resistivity by creating holes based on the Sn^{2+}/Sn^{4+} couple. Freshly prepared samples using the solution method were employed using isopropanol graphite suspension to make the electrical contacts. This was found to be a necessary precaution to avoid possible redox effects resulting from direct contact of the material with a metal surface. Single-crystals prepared from the solution method (0.1–1 mm length) and cold-pressed pellets from the annealing method ($1.67 \times 1.67 \times 5.00$ mm^3) were investigated. In both cases, the samples were found to have a significant resistivity showing a semiconducting behavior. By contrast, when the open tube method was employed, the solids obtained had a much lower resistivity behaving as *p*-type "metals". The samples were measured using both a PPMS 4-probe setup for low temperature data (5–330 K) and a conventional 4-probe method for room and high temperature measurements (300–550 K). The measured resistivity displays a tendency to decrease after every measurement cycle until it reaches an equilibrium value after several cycles which remains constant. This behavior can be attributed to contact annealing or similar effects. Such a behavior has also been observed in the case of $CsSnI_3$.[12] The resistivity values reported here correspond to the equilibrium resistivity values.

Low-Temperature Resistivity. Resistivity data were collected in the 5–330 K range for single-crystals of **1**–**3** (Figure 11) using the PPMS instrumentation where a similar behavior to the one described above was observed. The initial high resistivity values obtained at 5 K gradually decrease as the temperature increases and at ~330 K are 4 Ω cm for $CH_3NH_3SnI_3$, 34 Ω cm for $HC(NH_2)_2SnI_3$, and 596 Ω cm for $CH_3NH_3PbI_3$). This resistivity vs temperature trend is characteristic of undoped semiconductors. On cooling, resistivity increases again down to 5 K. However, the absolute values were observed to slightly decrease in the case of **1** and slightly increase in the case of **2** and **3** suggesting hysteretic behavior. This hysteresis comes as a consequence of the structural phase transitions. In fact, the structural phase transitions are reflected as anomalies in the resistivity close to the transition temperature. Thus, compound **1** changes to the *β*-phase in the 250 K region followed by one more transition to the *γ*-phase around 130 K. A resistivity increase around 70 K suggests more phase transitions on lowering the temperature. Similarly, for compounds **2** and **3** the *β*-phase is reached at 225 K and 320 K, respectively, while the *γ*-phase is observed at 110 K and 180 K, respectively. The transition temperatures are in good agreement with the transition observed in X-ray diffraction studies discussed above. In the case of **3** where the *α*/*β* phase transition occurs above room temperature, resistivity data were also collected in the 300–400 K region using the conventional setup (see Experimental Section), revealing a sharp transition with an onset at 310 K.

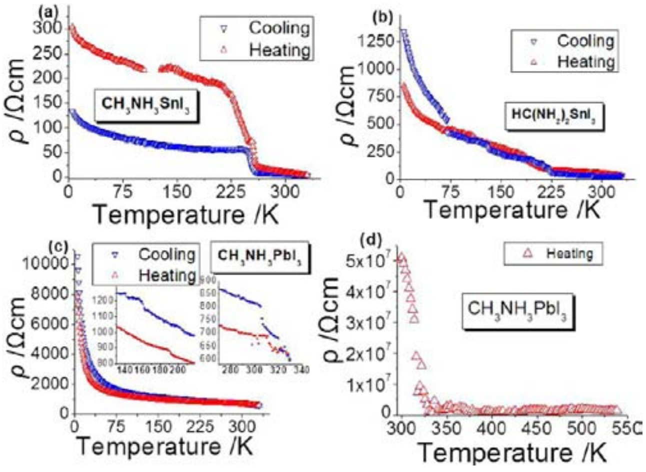

Figure 11. Single-crystal temperature-dependent resistivity plots of (a) $CH_3NH_3SnI_3$, (b) $HC(NH_2)_2SnI_3$, (c) $CH_3NH_3PbI_3$ in the 5–330 K temperature range (PPMS) and (d) $CH_3NH_3PbI_3$ in the 300–540 K range (MMR). The specimens were obtained from the solution method.

Room Temperature and High-Temperature Resistivity. Cold-pressed rectangular pellets ($1.67 \times 1.67 \times 5.00$ mm^3) of **1**–**4** prepared from powders of the ground samples annealed at 200 °C for 2 h in a sealed tube and/or elongated rhombic dodecahedral single-crystal ($0.5 \times 0.5 \times 0.5$ mm^3) of **1**–**3** prepared from the solution were also measured using the conventional 4-probe method (Supporting Information, Figure S10). A remarkable behavior can be easily spotted differentiating $CH_3NH_3PbI_3$ from its other perovskite counterparts. The difference lies in the strongly non-ohmic characteristics of **3** evident in the *I*–*V* curves of the measured materials (Supporting Information, Figure S10). The $CH_3NH_3SnI_3$, $HC(NH_2)SnI_3$ and $HC(NH_2)PbI_3$ compounds display a nearly perfect ohmic behavior with resistivity values of 0.49, 11.8 and 3.4×10^3 Ω cm at 300 K following a declining trend with increasing temperature.

$CH_3NH_3PbI_3$ is singled-out since it reproducibly displayed a non-ohmic behavior with a parabolic *I*–*V* dependence. The calculated resistivity value for a single-crystal of $CH_3NH_3PbI_3$, ignoring the nonlinear parts of the plot, is 51 MΩ·cm at room temperature. This resistivity value is in general agreement with the previously reported value of 6.6 MΩ·cm obtained for a polycrystalline sample.[46] The non-ohmic behavior of **3** is graphically highlighted in Figure 12c as the *I*–*V* curve completes a full hysteresis loop upon reversal of the current polarization. Interestingly, the resistivity value varies slightly with the polarity of the applied electric field with a higher slope being obtained for negative polarity. The equilibrium value of the voltage for zero applied current (remnant polarization) is roughly −10 mV, but in general displays a strong dependence on the crystal history. These characteristics strongly imply a ferroelectric response (the point group 4*mm* allows for such a behavior). The resistivity graphs of compounds **1**, **2**, and **4** on the contrary display normal ohmic behavior.

In terms of absolute resistivity there is a discrepancy between the low- and the high-temperature values for the single-crystalline samples. We rationalize this based on the *I*–*V* characteristics of **1**–**4** (Supporting Information, Figure S10). At room temperature, **1**, **2**, and **4a** which adopt the *α*-phase display nearly perfect ohmic behavior which results in resistivities in the 10^{0}–10^{1} Ω cm range for the Sn compounds and 10^3 Ω cm for the Pb compound. On the other hand, the *β*-phase of **3** displays a remarkable non-ohmic behavior which is responsible for a hysteresis loop obtained in its *I*–*V* plot. The hysteretic behavior can be attributed to the reorientation of the permanent dipoles of $CH_3NH_3^+$ on application of external electric field in addition to the resistance of the inorganic

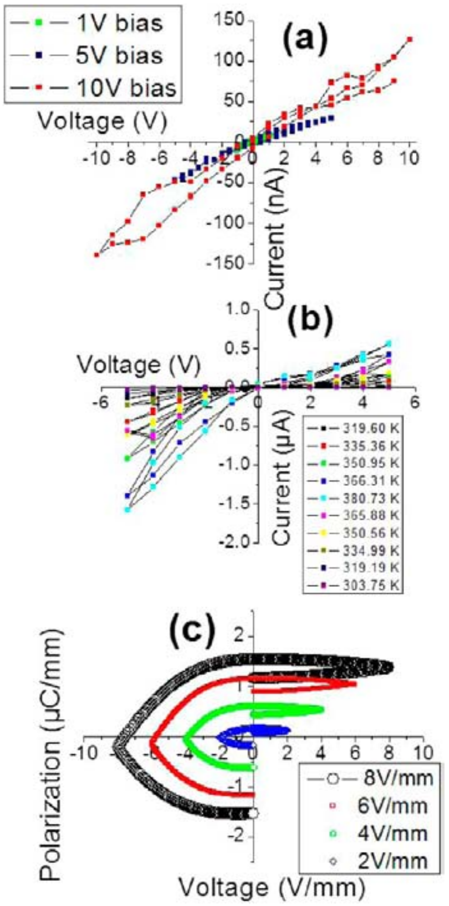

Figure 12. Hysteresis loops for a sample of compound **3**. (a) Voltage and (b) temperature dependence of the coercive field and (c) polarization as a function of applied bias. The measured specimen was prepared via the solution method.

$\{PbI_3\}^-$ lattice. This is clearly a ferroelectric response. Thus, a capacitance/inductance factor is introduced to the charge transport which reflects the ability of the permanent dipoles to align with the applied field while confined within the perovskite "cage". Field- and temperature-dependence of the coercive field in the $I-V$ hysteresis loops as well as polarization measurements also suggest a motion of charge within the material (Figure 12).

Thermopower. To assign the carrier type in the perovskite compounds, we performed Seebeck coefficient measurements on both solution derived single-crystals of **1**−**3** and cold-pressed pellets of **1**−**4** fabricated from powders of the ground samples annealed at 200 °C for 2 h (sealed tube). The compound $HC(NH_2)PbI_3$ could only be measured in the latter form, since the pressure applied to form the pellets (~10 GPa) was sufficient to stabilize the perovskite (black) form for several hours. The thermopower of the single crystals for compounds **2** and **3** in the 300−400 K range, (Figure 13) are negative and very large in magnitude indicating that the materials are *n*-type semiconductors with very low levels of electron carriers. The Seebeck coefficients were −2700 and −6500 μV/K at 380 K for **2** and **3**, respectively. These values are consistent with carrier concentration of $<10^{16}$ cm^{-3}. For compound **3**, the Seebeck value was sensitive to the phase transition, consistent with the overall change in the other transport properties.

To gain further insight into the transport characteristics, a complete collection of **1**−**4** and **5b** (vide infra) was prepared as cold-pressed from annealed powders obtained from the grinding method. All samples prepared this way had nearly identical geometric dimensions which allowed for a direct comparison of their electron transport properties. Interestingly, with the exception of **4a** which is *p*-type, all samples display a *n*-type behavior. The Pb-containing samples invariably show an extremely high Seebeck coefficient in the order of few (for **5b**) to several mV/K (for **3** and **4b**) indicative of very low carrier concentration. The polycrystalline pellets of the Sn-based compounds (including a sample of similarly prepared $CsSnI_3$) on the other hand show significantly lower Seebeck coefficients in the order of few hundreds of μV/K indicating a higher carrier concentration (still low as an absolute value) with respect to the Pb analogues (Figure 14). The samples still behave as

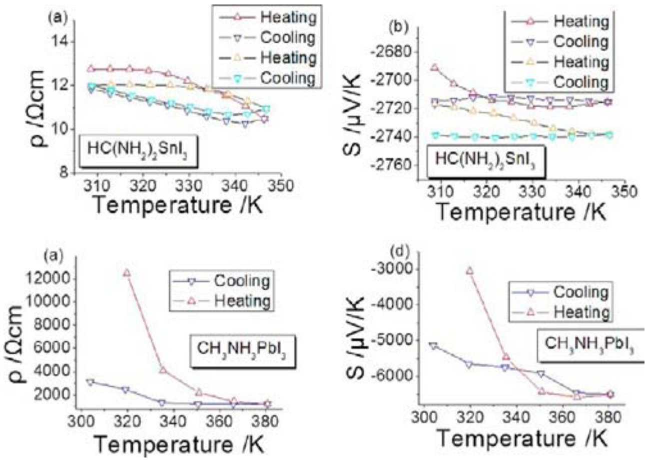

Figure 13. Temperature-dependence of the Seebeck coefficients on single-crystals of **2** (b) and **3** (d). The respective resistivity values are given for reference in panels (a) and (c). The single-crystals were obtained from the solution method.

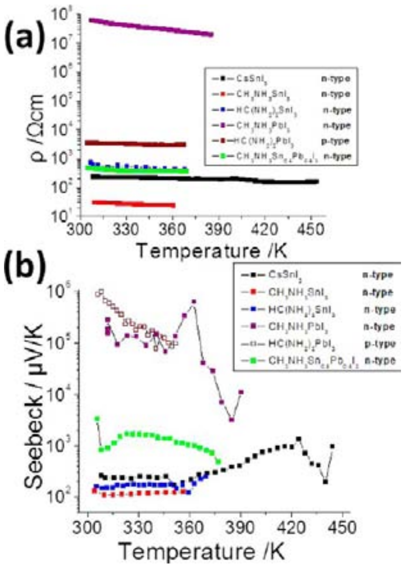

Figure 14. Temperature-dependence (a) resistivity and (b) Seebeck coefficients on cold-pressed pellets of annealed polycrystalline samples of the compounds **1**−**4**, **5b**, and a $CsSnI_3$ reference. The pellets were annealed for 2 h at 200 °C under vacuum prior to the measurement. Negative Seebeck coefficients were converted to positive to fit in the logarithmic scale. N-type compounds are named as such in the figure labels.

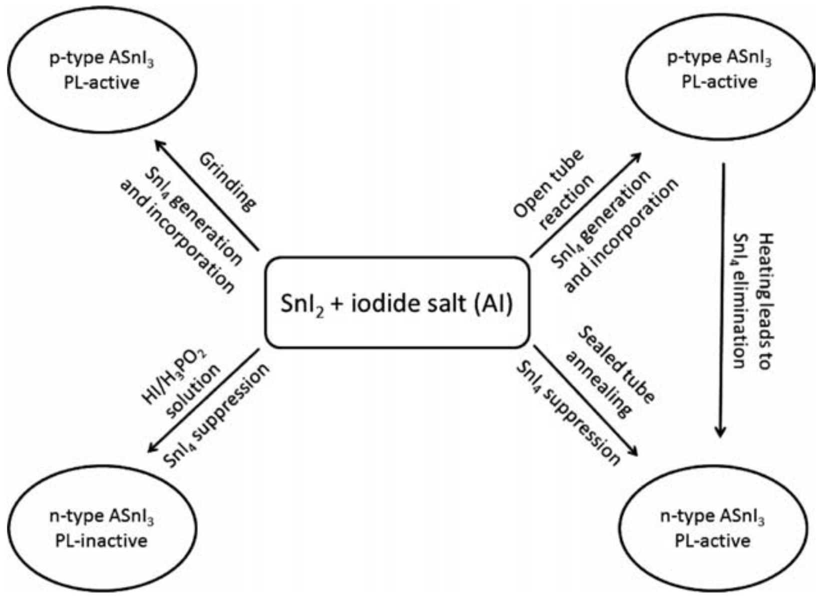

Figure 15. Carrier-type transformations and PL-emission relationships in $ASnI_3$ (A = Cs^+, $CH_3NH_3^+$ or $HC(NH_2)_2^+$) effected by the different synthetic methods employed.

semiconductors as evidenced by resistivity measurements. When the pressed pellets are made from samples that are not annealed, the Sn compounds are *p*-type semiconductors. A typical example of this *p*-type behavior is observed in $CsSnI_3$.[12] We have confirmed this *p*-type behavior on samples of **1** prepared from the open tube method (Supporting Information, Figure S11) which show a similar resistivity (24 Ω cm) and a small and positive value of the Seebeck coefficient (+82 μV/K). These values, although they clearly indicate the change of the carrier type on doping are still much higher than those previously reported for $CH_3NH_3SnI_3$[2i,8b] suggesting a lower level of doping.

Hall-Effect Measurements. Hall effect measurements also performed on cold-pressed pellets of annealed polycrystalline **1**−**3**, **5b**, and a reference sample of $CsSnI_3$ (prepared with the same method) to estimate the carrier concentration of the compounds. The specimens were measured under a variable magnetic field of 0.5−1.25 T under a constant excitation of 10 μA for the less resistive samples (**1**, **2**, **5b**) and 100 nA for compound **3** (Supporting Information, Figure S13). The Hall coefficients were negative and confirm the negative sign of the carriers (*n*-type) for all the thus prepared compounds. The carrier concentrations were determined based on the formula: $n = -B_zI_x/dV_He$, where B_z is the magnetic field, I_x is the electric current, d is the sample thickness, e is the charge of electron, and V_H is the Hall voltage. They were in the order of 10^{14} cm^{-3} for **1**, **2**, **5b** and a similarly prepared sample of $CsSnI_3$ while the respective carrier concentration for compound **3** was estimated at ~10^9 cm^{-3}. The data are in excellent agreement with the very large Seebeck coefficients (Figure 14b). The very low carrier concentrations correspond to nearly intrinsic semiconducting behavior. This finding is further corroborated by the fact that the specimens, except for *p*-type compound **4a**, do not display any PL signal after the measurements indicating depletion of the defects, which also give rise to the charge carriers. This is consistent with the proposal that the PL arises from Sn^{4+} centers present in dopant concentrations in the PL-active samples. The disappearance of PL is probably caused by the thermal treatment during sample preparation and several heating/cooling cycles during the measurements which significantly reduces Sn^{4+} centers as explained above. Combining resistivity and Hall effect data (measured for the same specimens), the electron mobility was calculated to be ~2320 cm^2/V·s for $CH_3NH_3SnI_3$, ~536 cm^2/V·s for $CsSnI_3$, ~103 cm^2/V·s for $HC(NH_2)_2SnI_3$, ~270 cm^2/V·s for $CH_3NH_3Sn_{0.5}Pb_{0.5}I_3$, and ~66 cm^2/V·s for $CH_3NH_3PbI_3$ using the expression $\mu = 1/ne\rho$. These are remarkably high values and are comparable to those of classical semiconductors including Si, GaAs, InP, and so forth. Such values for carrier mobility are also consistent with the previously reported values for $CsSnI_3$.[12] The hole carrier mobility for the *p*-type sample of $CH_3NH_3SnI_3$ prepared from the open tube method was found to be ~322 cm^2/V·s (carrier concentration ~10^{15}), significantly lower than the electron mobility, but still comparable to the value obtained for *p*-type $CsSnI_3$, ~520 cm^2/V·s.[12]

Our present experimental charge transport results are quite different from those reported previously. For example, the resistivity for $CH_3NH_3SnI_3$ is higher by at least one[2i] or two[8b] orders of magnitude from previously reported samples (for both *p*- and *n*-type specimens), and this is attributed to the differences in the synthetic approach, as discussed above. More importantly, we find that the overall assessment of the Sn compounds as *p*-type "metals" needs to be revised since our results clearly indicate that $CH_3NH_3SnI_3$ and $HC(NH_2)_2SnI_3$ can behave as *n*-type semiconductors. The reason for the ability of these compounds to be *p*-type conductors (e.g., as in the case of $CsSnI_3$) is the unique property of the materials to accommodate Sn^{4+} centers and thus to transition to a doped state with charge carriers being holes. In this work we were able to achieve samples with a very low carrier concentrations and defects because of the presence of a powerful reducing agent (i.e., H_3PO_2) which inhibits/reverses the self-doping process (i.e., suppress formation of Sn^{4+}) and allows the isolation of the pure stoichiometric compounds. *P*-type conducting behavior is observed when the preparation of the Sn compounds is carried out through solid-state methods. The absence of the reducing agent renders the Sn^{2+}/Sn^{4+} conversion irreversible and therefore the obtained solids are inherently doped. The fact

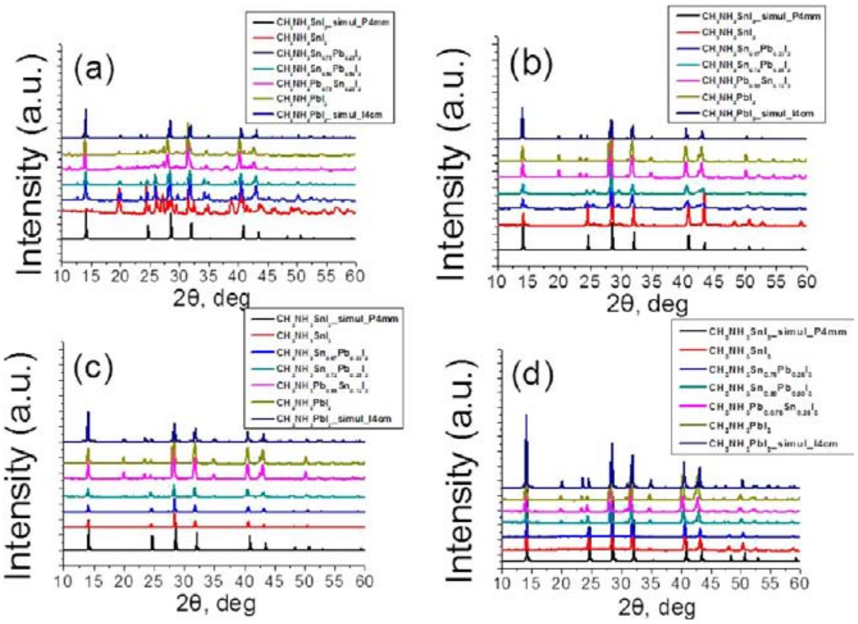

Figure 16. X-ray powder diffraction patterns of $CH_3NH_3Sn_{1-x}Pb_xI_3$ solid solution as obtained from (a) grinding, (b), open tube melt, (c) sealed tube annealing, and (d) solution reactions. In the cases where there is ambiguity on the Sn:Pb ratio the values were obtained from EDS analysis.

that Sn oxidation is responsible for the "metal-like" behavior in the solid state is highlighted by a direct comparison with the Pb-analogues (which cannot undergo analogous Pb^{2+}/Pb^{4+} doping because of the instability of Pb^{4+} in an iodide coordination environment). In the latter system, the charge transport properties are practically unaffected by the preparative route.

Interestingly, it is still possible to "un-dope" the semiconductors to a nearly carrier-depleted *n*-type state. This can be achieved with extensive thermal treatment at ∼200 °C, at which temperature Sn^{4+} dopants are eliminated in the form of volatile SnI_4. Excess of the organic cations can also be partially removed at the annealing temperature in the form of the free amine and HI gas. Therefore the doping levels within the Sn-based materials are controllable simply by choosing the appropriate synthetic method to generate *p*- or *n*-type semiconductors in the $ASnI_3$ family of compounds. A schematic representation of the carrier type transformations is given in Figure 15.

In addition, the above results illustrate that the phase transitions determine the transport characteristics of the semiconducting perovskite compounds. In their highest symmetry (α-phase), the perovskites display the maximum conductivity, which is a consequence of the maximum orbital overlap between the metal and the iodine (linear Sn−I−Sn bond). As the phase transitions progress at lower temperatures (β- and γ-phases) the change in the M−I−M angles result in reduced orbital overlap, thus hindering the charge transport through the inorganic framework. This trend is nicely illustrated by the symmetry lowering which is $CH_3NH_3SnI_3$ (C_{4v}) > $CsSnI_3$ (D_{2h}) > $HC(NH_2)_2SnI_3$ (C_{2v}) and $HC(NH_2)_2PbI_3$ (C_{3v}) > $CH_3NH_3PbI_3$ (C_{4v}) > $CsPbI_3$ (C_{2h}) for the Sn-series and Pb-series, respectively (Schönflies symmetry is given in parentheses). This trend is also reflected in the band gap evolution throughout the series. The transport properties of β-$CH_3NH_3PbI_3$, in particular, where a capacitor-like behavior was observed, may be rationalized by the reorientation of the $CH_3NH_3^+$ dipoles on application of current through the material, which mask the properties of the inorganic $[PbI_3]^-$ framework.

$CH_3NH_3Sn_{1-x}Pb_xI_3$ Solid Solution Studies. In the context of the above results, we decided to study the properties of $CH_3NH_3Sn_{1-x}Pb_xI_3$ solid solutions to explore the structure and property trends as a function of *x*. As shown above, these two phases follow the same phase transition path, albeit the transitions occur at different temperatures. The materials were studied as a function of the preparation route as described above. Powder X-ray diffraction patterns are presented in Figure 16.

The X-ray powder diffraction patterns show that the ground samples contain impurities. The other three preparative methods (open tube melting, sealed tube annealing, solution) provide sufficiently pure materials. The weak Bragg reflections observed near the triplet of major peaks at 24.7°, 28.6°, and 32.1° 2θ angles have been discussed earlier in the context of Figure 2b as an oxidation impurity. For materials prepared from the melt the three peaks appear already at the onset of data collection. For samples obtained from solution synthesis and the annealed samples the minor reflections appear in the powder diffraction patterns only after prolonged exposure in air during data collection. The cleanest pattern was obtained from the annealed samples because of strong diffraction requiring a considerably shorter collection time, so that substantial oxidation does not occur. Therefore, it is clear that these reflections are due to oxidation of Sn in the compounds since they do not appear in the diffraction patterns of corresponding pure Pb and Pb-rich phases.

The lattice parameters calculated from the diffraction patterns obtained from the annealed samples (Figure 15c), are given in the Supporting Information, Table S25. The evolution of the structure in this solid solution system is consistent, irrespective of the method used. The Sn-rich compositions adopt the pseudocubic tetragonal *P4mm* structure of the parent α-$CH_3NH_3SnI_3$ compound up to $x = 0.5$. For $x > 0.5$ the structure changes to that of the tetragonal β-$CH_3NH_3PbI_3$, *I4cm*. It must be noted here that the volume

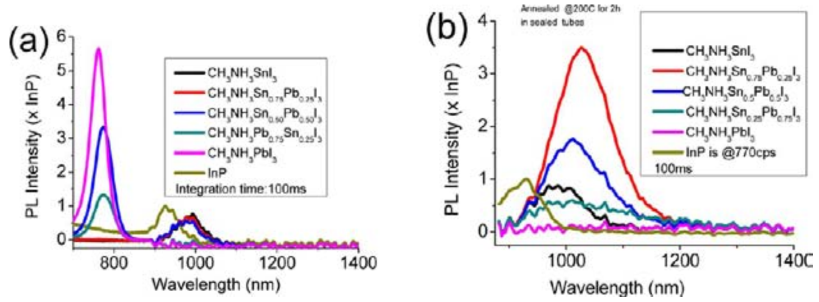

Figure 17. PL properties of $CH_3NH_3Sn_{1-x}Pb_xI_3$ solid solution as obtained from (a) mildly grinding the precursors (interface reaction) and (b) by annealing the same specimen at 200 °C for 2 h in a sealed tube. The data are normalized toward single crystalline InP.

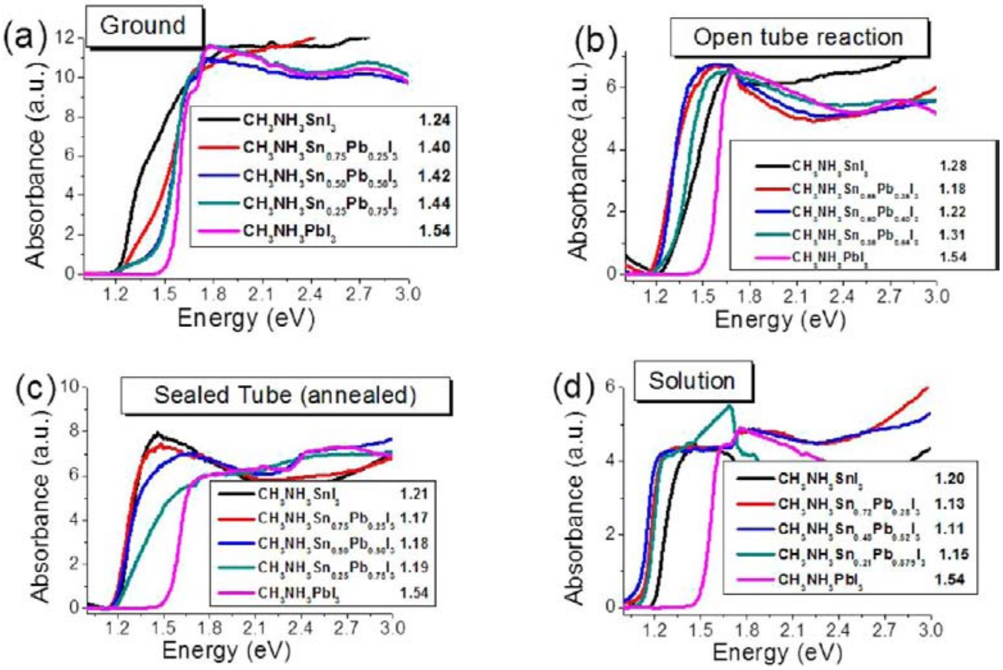

Figure 18. Optical absorption properties of $CH_3NH_3Sn_{1-x}Pb_xI_3$ solid solution as obtained from (a) grinding, (b), open tube melt, (c) sealed tube annealing, and (d) solution reactions. In the cases where there is ambiguity on the Sn:Pb ratio the values were obtained from EDS analysis. The value of the band gap is given next to each composition.

of the unit cell in the series changes only slightly, which is consistent with previous observations that the cell dimensions are dictated by the nature of the halide ions.[47]

The PL properties of $CH_3NH_3Sn_{1-x}Pb_xI_3$ are strongly affected by mixing the Sn and Pb sites (Figure 17). Again, materials prepared from solution were not luminescent. The mixed-metal perovskites prepared from the melt were also inactive, in contrast to the pure phases prepared by the same method for $x = 0$ and $x = 1$. Intense PL was produced only when the materials were prepared by mild grinding so that some unreacted solid remains (interface reaction). The PL intensity decreases as the mixture is thoroughly ground to a visually homogeneous black powder and the reaction is almost complete. The emission observed from this process corresponds to the individual Sn and Pb centers showing two peaks at the respective emission wavelengths (Figure 10a). However, when the material is placed in a sealed tube and annealed at 200 °C, the formation of the solid solution is complete, and the Sn and Pb active centers are fully mixed. As a result, the initial emission peaks disappeared, and a new red-shifted peak appeared for $x = 0.25$ at 1030 nm. This is an overall red shift of 70 nm with respect to the end member $CH_3NH_3SnI_3$ (Figure 10b). For $x > 0.25$ the shift is smaller as is the intensity of the peak. Generally, the intensity seems to slightly decrease by annealing.

The red shift in the emission wavelength is reflected in the electronic absorption UV−vis spectra which universally show a shift of the band gap to lower energies (Figure 18). The largest band gap shift occurs in the materials obtained from solution, on the Pb-rich side of the compositions reaching values of 1.1 eV (Figure 19). However, no emission could be detected in these specimens. The annealed materials show an excellent agreement between absorption energy and emission wavelength and may indeed prove valuable in tuning the emission properties of the iodide perovskites.

■ CONCLUDING REMARKS

A broad family of hybrid Sn and Pb iodide compounds with semiconducting properties bearing methylammonium or formamidinium cations can be universally stabilized in the 3D perovskite structure type, AMX_3. The preparative route chosen for the materials is of utmost importance as it governs their respective physical properties. The structural properties of these phases strongly resemble the behavior of the perovskitic oxides

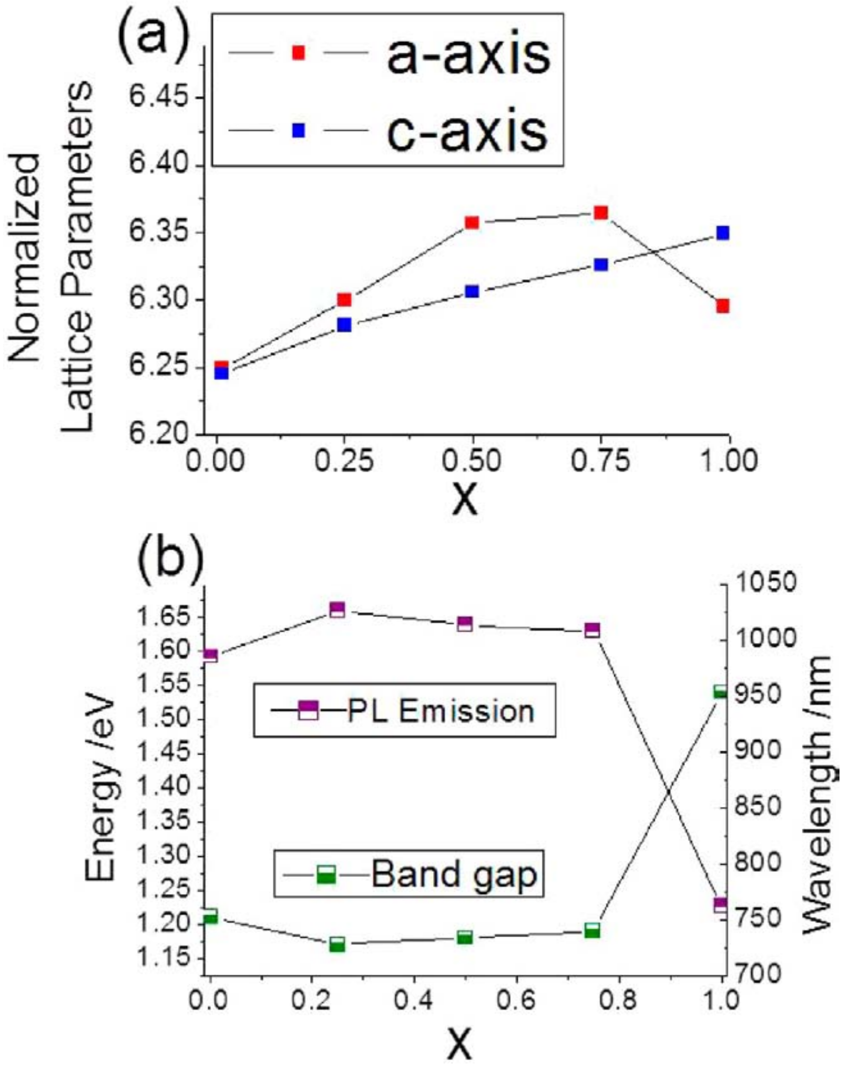

Figure 19. (a) Normalized lattice constants and (b) optical properties of $CH_3NH_3Sn_{1-x}Pb_xI_3$ as a function of composition from the samples obtained through sealed tube annealing of ground samples showing the evolution of PL emission wavelength and the energy band gap. The normalization factor is $\sqrt{2}/2$ and 1/2 for *a*- and *c*-axis, respectively.

by undergoing reversible, temperature-dependent phase transitions. The electrical properties can be controlled to a large extent by selecting the preparation method or the thermal treatment. The entire family featured direct energy gaps spanning the range between 1.1 to 1.7 eV. This makes them highly relevant as possible light absorbers in energy conversion or detector devices. The Pb and Sn containing members of the family display strong PL at room temperature which is superior to classical semiconducting materials such as InP, but in addition, the emission wavelength can be shifted through subtle changes in their compositions. Transport properties confirm the semiconducting nature of the compounds showing additionally strong dependence upon structural changes. In the case of β-$CH_3NH_3PbI_3$, a capacitor-like behavior was observed at room temperature which suggests that the other Sn and Pb analogues might show similar behavior upon transitioning into the β-phase. Overall, we consider the hybrid iodide perovskites as flexible multipurpose functional materials emitting in the near-IR spectral region at room temperature. They are easily accessible and scalable and display remarkable charge transport, optical absorption, and room temperature PL properties. The lower the number of defects in the structure, the lower is the ability to exhibit PL. Our findings open a path for deeper understanding and further development of these materials as components in various applications. The ability to be a good electrical conductor and strong emitter at room temperature is a remarkable characteristic which places these materials in an elite class of solution processable semiconductors. Although the initial studies of the materials date back to the 1970s, their complex behavior, exotic properties, and chemical and physical subtleties are only now beginning to be understood. The interplay between *p*- and *n*-type semiconducting behavior due to the presence or elimination of the Sn^{4+} dopant is a characteristic example of this complexity and versatility in the chemistry and physics of the hybrid metal iodide perovskites. The suitable energy band gaps and impressively large carrier mobilities reported here and in previous publications on $CsSnI_3$[12,15] and $CH_3NH_3PbI_3$[15a,b,d,e] indicate that these materials are very promising for modern energy-related applications, such as solar energy conversion, as we have shown for example in the case of $CsSnI_3$.[15c] Future work should be focused on optimization of the PL intensity and fabrication of thin films for use in devices.

■ ASSOCIATED CONTENT

Supporting Information

Atomic coordinates and anisotropic thermal factors for compounds **1**−**7**, as well as supplementary X-ray diffraction, thermal, and spectroscopic data. This material is available free of charge via the Internet at http://pubs.acs.org.

■ AUTHOR INFORMATION

Corresponding Author

*E-mail: m-kanatzidis@northwestern.edu.

Notes

The authors declare no competing financial interest.

■ ACKNOWLEDGMENTS

We thank OmniPV, Inc. for providing us with the instrumentation for the measurement of the PL properties. This work was supported in part from the ANSER Center, an Energy Frontier Research Center funded by the U.S. Department of Energy, Office of Science, Office of Basic Energy Sciences, under Award No. DE-SC0001059.

■ REFERENCES

(1) Kay, H. F.; Bailey, P. C. *Acta Crystallogr.* **1957**, *10*, 219.

(2) (a) Moller, C. K. *Nature* **1957**, *180*, 981. (b) Moller, C. K. *Nature* **1958**, *182*, 1436. (c) Moller, C. K. *Mat. Fys. Medd. Dan. Vid. Selsk.* **1959**, 32. (d) Weber, D. *Z. Naturforsch.* **1978**, *33b*, 862. (e) Weber, D. *Z. Naturforsch.* **1978**, *33b*, 1443. (f) Yamada, K.; Tsuritani, T.; Okuda, T.; Ichiba, S. *Chem. Lett.* **1989**, *18*, 1325. (g) Yamada, K.; Funabiki, S.; Horimoto, H.; Matsui, T.; Okuda, T.; Ichiba, S. *Chem. Lett.* **1991**, *20*, 801. (h) Trots, D. M.; Myagkota, S. V. *J. Phys. Chem. Solids* **2008**, *69*, 2520. (i) Takahashi, Y.; Obara, R.; Lin, Z.-Z.; Takahashi, Y.; Naito, T.; Inabe, T.; Ishibashi, S.; Terakura, K. *Dalton Trans.* **2011**, *40*, 5563. (j) Yamada, K.; Nakada, K.; Takeuchi, Y.; Nawa, K.; Yamane, Y. *Bull. Chem. Soc. Jpn.* **2011**, *84*, 926.

(3) (a) Papavassiliou, G. C.; Patsis, A. P.; Lagouvardos, D. J.; Koutselas, I. B. *Synth. Met.* **1993**, *57*, 3889. (b) Papavassiliou, G. C.; Koutselas, I. B. *Synth. Met.* **1995**, *71*, 1713. (c) Mitzi, D. B. *Chem. Mater.* **1996**, *8*, 791. (d) Guan, J.; Tang, Z.; M. Guloy, A. *Chem. Commun.* **1999**, 1833. (e) Kagan, C. R.; Mitzi, D. B.; Dimitrakopoulos, C. D. *Science* **1999**, *286*, 945. (f) Mitzi, D. B.; Dimitrakopoulos, C. D.; Kosbar, L. L. *Chem. Mater.* **2001**, *13*, 3728. (g) Tang, Z.; Guan, J.; Guloy, A. M. *J. Mater. Chem.* **2001**, *11*, 479. (h) Knutson, J. L.; Martin, J. D.; Mitzi, D. B. *Inorg. Chem.* **2005**, *44*, 4699. (i) Sakai, K.-i.; Sonoyama, T.; Tsuzuki, T.; Ichikawa, M.; Taniguchi, Y. *Chem. Lett.* **2005**, *34*, 212. (j) Sourisseau, S.; Louvain, N.; Bi, W.; Mercier, N.; Rondeau, D.; Boucher, F.; Buzaré, J.-Y.; Legein, C. *Chem. Mater.* **2007**, *19*, 600. (k) Takahashi, Y.; Obara, R.; Nakagawa, K.; Nakano, M.; Tokita, J.-y.; Inabe, T. *Chem. Mater.* **2007**, *19*, 6312.

(4) (a) Wang, S.; Mitzi, D. B.; Feild, C. A.; Guloy, A. *J. Am. Chem. Soc.* **1995**, *117*, 5297. (b) Koutselas, I. B.; Mitzi, D. B.; Papavassiliou, G. C.; Papaioannou, G. J.; Krautscheid, H. *Synth. Met.* **1997**, *86*, 2171. (c) Mitzi, D. B.; Liang, K.; Wang, S. *Inorg. Chem.* **1998**, *37*, 321.

(5) (a) Vincent, B. R.; Robertson, K. N.; Cameron, T. S.; Knop, O. *Can. J. Chem.* **1987**, *65*, 1042. (b) Tudela, D.; J. Sanchez-Herencia, A.; Diaz, M.; Fernandez-Ruiz, R.; Menendez, N.; Tornero, J. D. *J. Chem. Soc., Dalton Trans.* **1999**, 4019.

(6) (a) Tang, Z.; Guloy, A. M. *J. Am. Chem. Soc.* **1998**, *121*, 452. (b) Krautscheid, H.; Vielsack, F. *J. Chem. Soc., Dalton Trans.* **1999**, 2731. (c) Lode, C.; Krautscheid, H. *Z. Anorg. Allg. Chem.* **2000**, *626*, 326. (d) Guloy, A. M.; Tang, Z.; Miranda, P. B.; Srdanov, V. I. *Adv. Mater.* **2001**, *13*, 833. (e) Lode, C.; Krautscheid, H. *Z. Anorg. Allg. Chem.* **2001**, *627*, 841. (f) Lode, C.; Krautscheid, H. *Z. Anorg. Allg. Chem.* **2001**, *627*, 1454. (g) Lode, C.; Krautscheid, H. *Z. Anorg. Allg. Chem.* **2007**, *633*, 1691. (h) Wolff, M.; Harmening, T.; Pöttgen, R.; Feldmann, C. *Inorg. Chem.* **2009**, *48*, 3153. (i) Zhao, H.-R.; Li, D.-P.; Ren, X.-M.; Song, Y.; Jin, W.-Q. *J. Am. Chem. Soc.* **2009**, *132*, 18. (j) Li, H.-H.; Chen, Z.-R.; Cheng, L.-C.; Wang, Y.-J.; Feng, M.; Wang, M. *Dalton Trans.* **2010**, *39*, 11000.

(7) (a) Papavassiliou, G. C. *Prog. Solid State Chem.* **1997**, *25*, 125. (b) Mitzi, D. B. In *Progress in Inorganic Chemistry*; John Wiley & Sons, Inc.: New York, 2007; p 1; (c) Billing, D. G.; Lemmerer, A. *CrystEngComm* **2009**, *11*, 1549. (d) Mercier, N.; Louvain, N.; Bi, W. *CrystEngComm* **2009**, *11*, 720. (e) Wu, L.-M.; Wu, X.-T.; Chen, L. *Coord. Chem. Rev.* **2009**, *253*, 2787.

(8) (a) Mitzi, D. B.; Feild, C. A.; Harrison, W. T. A.; Guloy, A. M. *Nature* **1994**, *369*, 467. (b) Mitzi, D. B.; Feild, C. A.; Schlesinger, Z.; Laibowitz, R. B. *J. Solid State Chem.* **1995**, *114*, 159.

(9) (a) Mitzi, D. B.; Wang, S.; Feild, C. A.; Chess, C. A.; Guloy, A. M. *Science* **1995**, *267*, 1473. (b) Mitzi, D. B.; Liang, K. *J. Solid State Chem.* **1997**, *134*, 376.

(10) Calabrese, J.; Jones, N. L.; Harlow, R. L.; Herron, N.; Thorn, D. L.; Wang, Y. *J. Am. Chem. Soc.* **1991**, *113*, 2328.

(11) Mizusaki, J.; Arai, K.; Fueki, K. *Solid State Ionics* **1983**, *11*, 203.

(12) Chung, I.; Song, J.-H.; Im, J.; Androulakis, J.; Malliakas, C. D.; Li, H.; Freeman, A. J.; Kenney, J. T.; Kanatzidis, M. G. *J. Am. Chem. Soc.* **2012**, *134* (20), 8579.

(13) Chondroudis, K.; Mitzi, D. B. *Chem. Mater.* **1999**, *11*, 3028.

(14) Tanaka, K.; Takahashi, T.; Ban, T.; Kondo, T.; Uchida, K.; Miura, N. *Solid State Commun.* **2003**, *127*, 619.

(15) (a) Kojima, A.; Teshima, K.; Shirai, Y.; Miyasaka, T. *J. Am. Chem. Soc.* **2009**, *131*, 6050. (b) Im, J.-H.; Lee, C.-R.; Lee, J.-W.; Park, S.-W.; Park, N.-G. *Nanoscale* **2011**, *3*, 4088. (c) Chung, I.; Lee, B.; He, J.; Chang, R. P. H.; Kanatzidis, M. G. *Nature* **2012**, *485*, 486. (d) Etgar, L.; Gao, P.; Xue, Z.; Peng, Q.; Chandiran, A. K.; Liu, B.; Nazeeruddin, M. K.; Grätzel, M. *J. Am. Chem. Soc.* **2012**, *134*, 17396. (e) Lee, M. M.; Teuscher, J.; Miyasaka, T.; Murakami, T. N.; Snaith, H. J. *Science* **2012**, *338*, 643.

(16) Hang, T.; Zhang, W.; Ye, H.-Y.; Xiong, R.-G. *Chem. Soc. Rev.* **2011**, *40*, 3577.

(17) Mitzi, D. B. *J. Mater. Chem.* **2004**, *14*, 2355.

(18) Scaife, D. E.; Weller, P. F.; Fisher, W. G. *J. Solid State Chem.* **1974**, *9*, 308.

(19) (a) Shum, K.; Chen, Z.; Qureshi, J.; Yu, C.; Wang, J. J.; Pfenninger, W.; Vockic, N.; Midgley, J.; Kenney, J. T. *Appl. Phys. Lett.* **2010**, *96*, 221903. (b) Yu, C.; Chen, Z.; Wang, J. J.; Pfenninger, W.; Vockic, N.; Kenney, J. T.; Shum, K. *J. Appl. Phys.* **2011**, *110*, 063526. (c) Chen, Z.; Yu, C.; Shum, K.; Wang, J. J.; Pfenninger, W.; Vockic, N.; Midgley, J.; Kenney, J. T. *J. Lumin.* **2012**, *132*, 345.

(20) (a) Poglitsch, A.; Weber, D. *J. Chem. Phys.* **1987**, *87*, 6373. (b) Xu, Q. E., T.; Nakayama, H.; Nakamura, N.; Kishita, M. *Z. Naturforsch.* **1991**, *46a*, 240. (c) Onoda-Yamamuro, N.; Yamamuro, O.; Matsuo, T.; Suga, H. *J. Phys. Chem. Solids* **1992**, *53*, 277.

(21) Howie, R. A.; Moser, W.; Trevena, I. C. *Acta Crystallogr., Sect. B* **1972**, *28*, 2965.

(22) (a) Kortüm, G.; Braun, W.; Herzog, G. *Angew. Chem.* **1963**, *75*, 653. (b) McCarthy, T. J.; Tanzer, T. A.; Kanatzidis, M. G. *J. Am. Chem. Soc.* **1995**, *117*, 1294. (c) Larson, P.; Mahanti, S. D.; Kanatzidis, M. G. *Phys. Rev. B* **2000**, *61*, 8162. (d) Trikalitis, P. N.; Rangan, K. K.; Bakas, T.; Kanatzidis, M. G. *J. Am. Chem. Soc.* **2002**, *124*, 12255.

(23) Pfenninger, W. *OmniPV_PL*; OmniPV Inc, 2008

(24) Sheldrick, G. *Acta Crystallogr., Sect. A* **2008**, *64*, 112.

(25) Spek, A. *J. Appl. Crystallogr.* **2003**, *36*, 7.

(26) Farrugia, L. *J. Appl. Crystallogr.* **1999**, *32*, 837.

(27) Petricek, V.; Dusek, M.; Palatinus, L. *Jana2006, The crystallographic computing system*; Institute of Physics: Praha, Czech Republic, 2006.

(28) Stokes, H. T.; Hatch, D. M.; Campbell, B. J. *ISOTROPY*; Department of Physics and Astronomy, Brigham Young University: Provo, Utah, 2007; stokes.byu.edu/isotropy.html.

(29) Schaefer, F. C.; Hechenbleikner, I.; Peters, G. A.; Wystrach, V. P. *J. Am. Chem. Soc.* **1959**, *81*, 1466.

(30) Bedlivy, D.; Mereiter, K. *Acta Crystallogr., Sect. B* **1980**, *36*, 782.

(31) Fan, L.-Q.; Wu, J.-H. *Acta Crystallogr., Sect. E* **2007**, *63*, i189.

(32) (a) Howard, C. J.; Stokes, H. T. *Acta Crystallogr., Sect. B* **1998**, *54*, 782. (b) Howard, C. J.; Stokes, H. T. *Acta Crystallogr., Sect. B* **2004**,

60, 674. (c) Howard, C. J.; Stokes, H. T. *Acta Crystallogr., Sect. A* **2005**, *61*, 93.

(33) (a) Nord, G. L. *Phase Transitions* **1994**, *48*, 107. (b) White, T. J.; Segall, R. L.; Barry, J. C.; Hutchison, J. L. *Acta Crystallogr., Sect. B* **1985**, *41*, 93.

(34) Glazer, A. *Acta Crystallogr., Sect. B* **1972**, *28*, 3384.

(35) Swainson, I.; Chi, L.; Her, J.-H.; Cranswick, L.; Stephens, P.; Winkler, B.; Wilson, D. J.; Milman, V. *Acta Crystallogr., Sect. B* **2010**, *66*, 422.

(36) Mauersberger, P.; Huber, F. *Acta Crystallogr., Sect. B* **1980**, *36*, 683.

(37) Landau, L. D., Lifshitz, E. M. *Statistical Physics*, Part 1, 3rd ed.; Elsevier: Amsterdam, The Netherlands, 1980.

(38) Gesi, K. *Ferroelectrics* **1997**, *203*, 249.

(39) Wasylishen, R. E.; Knop, O.; Macdonald, J. B. *Solid State Commun.* **1985**, *56*, 581.

(40) (a) Mashiyama, H.; Kurihara, Y.; Azetsu, T. *J. Korean Phys. Soc.* **1998**, *32*, S156. (b) Kawamura, Y.; Mashiyama, H.; Hasebe, K. *J. Phys. Soc. Jpn.* **2002**, *71*, 1694. (c) Mashiyama, H.; Kawamura, Y.; Kasano, H.; Asahi, T.; Noda, Y.; Kimura, H. *Ferroelectrics* **2007**, *348*, 182.

(41) Maaej, A.; Bahri, M.; Abid, Y.; Jaidane, N.; Lakhdar, Z. B.; Lautié, A. *Phase Transitions* **1998**, *64*, 179.

(42) Baikie, T.; Fang, Y.; Kadro, J. M.; Schreyer, M.; Wei, F.; Mhaisalkar, S. G.; Graetzel, M.; White, T. J. *J. Mater. Chem.* **2013**, *1*, 5628.

(43) (a) Borriello, I.; Cantele, G.; Ninno, D. *Phys. Rev. B* **2008**, *77*, 235214. (b) Chang, H., Y.; Park, H., C.; Matsuishi, K. *J. Korean Chem. Soc.* **2004**, *44*, 5.

(44) Shockley, W.; Queisser, H. J. *J. Appl. Phys.* **1961**, *32*, 510.

(45) (a) Rau, U.; Glaeser, G. C. In *Photovoltaic Energy Conversion, Conference Record of the 2006 IEEE 4th World Conference*, 2006; Vol. *1*, p 205; (b) Slooff, L. H.; Bende, E. E.; Burgers, A. R.; Budel, T.; Pravettoni, M.; Kenny, R. P.; Dunlop, E. D.; Büchtemann, A. *Phys. Status. Solidi RRL* **2008**, *2*, 257.

(46) Knop, O.; Wasylishen, R. E.; White, M. A.; Cameron, T. S.; Oort, M. J. M. V. *Can. J. Chem.* **1990**, *68*, 412.

(47) Clark, S. J.; Donaldson, J. D.; Harvey, J. A. *Chem. Mater.* **1995**, *5*, 1813.